

This Dissertation

entitled

SOME TITLE

typeset with NDdiss2 ϵ v3.2013 (2013/04/16) on April 27, 2018 for

Michael Thaddeus Moran

This L^AT_EX 2 ϵ classfile conforms to the University of Notre Dame style guidelines as of Fall 2012. However it is still possible to generate a non-conformant document if the instructions in the class file documentation are not followed!

Be sure to refer to the published Graduate School guidelines at <http://graduateschool.nd.edu> as well. Those guidelines override everything mentioned about formatting in the documentation for this NDdiss2 ϵ class file.

It is YOUR responsibility to ensure that the Chapter titles and Table caption titles are put in CAPS LETTERS. This classfile does *NOT* do that!

This page can be disabled by specifying the “noinfo” option to the class invocation. (i.e., \documentclass[... ,noinfo]{nddiss2e})

This page is *NOT* part of the dissertation/thesis. It should be disabled before making final, formal submission, but should be included in the version submitted for format check.

NDdiss2 ϵ documentation can be found at these locations:

<http://www.gsu.nd.edu>
<http://graduateschool.nd.edu>

SOME TITLE

A Dissertation

Submitted to the Graduate School
of the University of Notre Dame
in Partial Fulfillment of the Requirements
for the Degree of

Doctor of Philosophy

by

Michael Thaddeus Moran

Manoël Couder, Co-Director

Michael C. F. Wiescher, Co-Director

Graduate Program in Physics

Notre Dame, Indiana

April 2018

SOME TITLE

Abstract

by

Michael Thaddeus Moran

The St. George recoil separator is currently undergoing its final commissioning work to fully characterize it ahead of the first experimental campaign to study (α, γ) reactions of astrophysical interest. The work currently completed to that end and comparison to the expected operation will be discussed. A single campaign utilizing the first two main sections of St. George to study two strong resonances in the $^{27}\text{Al}(p, \alpha)^{24}\text{Mg}$ has been completed as an initial test of the combined angular and energy acceptance of the separator, the rejection properties of the Wien filter, and the exploration of the use of St. George for studying other astrophysically important reaction types. The results and comparison to accepted values will be presented alongside the extensions to other reactions and considerations for extending the analysis capabilities of the separator.

To Laura, my rock.

CONTENTS

FIGURES	vi
TABLES	vii
CHAPTER 1: INTRODUCTION	1
1.1 Astrophysically-important Reaction Channels	1
1.2 Beam Optics	2
1.3 Recoil Mass Separation	2
1.3.1 Motivation	3
1.3.2 Background Sources	4
1.3.2.1 Detection System	5
1.3.3 Recoil Separators	6
1.3.3.1 CalTech Separator	6
1.3.3.2 ARES	7
1.3.3.3 DRAGON	7
1.3.3.4 ERNA	8
1.3.3.5 St. GEORGE	8
CHAPTER 2: EXPERIMENTAL SETUP	9
2.1 The St. Ana Accelerator and Transport Line	9
2.2 The St. George Recoil Separator	11
2.2.1 Subsections of St. George	12
2.2.2 Diagnostic Equipment	15
2.3 Detector System and Data Acquisition	17
2.4 Target Chamber	18
CHAPTER 3: COMMISSIONING ST. GEORGE	20
3.1 Theoretical and Experimental Considerations	21
3.2 Separator Properties	25
3.2.1 Magnetic Fringe Fields and Effective Field Lengths	26
3.3 Energy and Angular Acceptance	30
3.3.1 Beam Tuning and Properties	31
3.3.1.1 Before St. George	33
3.3.1.2 Within St. George	38
3.3.1.3 Collimator and Target Position	41

3.3.2	Energy Acceptance	42
3.3.3	Angular Acceptance	44
3.4	Considerations	47
CHAPTER 4: MEASURING THE $^{27}\text{Al}(\text{p}, \alpha)^{24}\text{Mg}$ CROSS SECTION		49
4.1	Altered Tune	49
4.2	Experimental Considerations	50
4.2.1	Beam Reduction	50
4.3	Procedure	52
4.3.1	Campaign Procedure	52
4.3.2	Run Procedure	52
4.4	Data Reduction and Analysis	53
4.4.1	Experimental Systematics	53
4.4.1.1	Target Properties	53
4.4.1.2	Detector Properties	55
4.4.1.3	Separator Properties	56
4.4.2	Yield Extraction	58
4.5	Detector Spectrum Verification	61
4.5.1	Assumptions	62
4.5.2	Required SRIM Files	63
4.5.3	Simulating the reaction	64
4.5.3.1	Simulating the incident beam	64
4.5.3.2	Simulating the produced particles	66
4.5.3.3	Detector spectrum comparison	66
4.5.4	SRIM Results	67
CHAPTER 5: ANALYSIS		68
5.1	Target Properties	68
5.2	Beam Properties	71
5.3	Detector Properties	72
5.4	Additional Parameters	74
5.5	Final Acceptance Measurements	75
CHAPTER 6: Discussion and Conclusion		78
6.1	Uncertainties	78
6.2	Uniformity of Acceptances	80
6.3	Potential Sources of Error	81
6.4	The (p, α_1) channel	81
6.5	Requirements for Replication and Improvement	82
6.6	Next Steps	82
6.7	Closing Thoughts	82
APPENDIX A: POLE TIP FIELDS		83

APPENDIX B: RUN INFORMATION	84
APPENDIX C: DEFLECTOR SETTINGS	86
APPENDIX D: ANALYSIS PACKAGE	88
D.1 Python for Nuclear Experiments	89
D.2 St. George Analysis Package	89
D.3 Justification	89
BIBLIOGRAPHY	91

FIGURES

2.1	Layout of the St. George recoil separator	13
3.1	Horizontal and vertical rays through St. George	22
3.2	Normalized field with Enge fit	28
3.3	Comparison between fringe fields	30
3.4	Designed $B\rho - E\rho$ rigidity phase space for St. George	32
3.5	Sketch of beam divergence due to focusing strength	33
3.6	Sketch of quadrupole steering of misaligned beam	36
4.1	Target thickness measurement	54
4.2	Detector response example	56
4.3	Possible proton peak	60

TABLES

3.1	ENGE COEFFICIENTS FOR Q_{10} COMPARED TO COSY DEFAULTS	29
4.1	POLE TIP FIELDS FOR (α, γ) AND (p, α) STUDIES	51
4.2	ALPHA PARTICLE PROPERTIES	52
4.3	ALPHA PARTICLE ENERGIES FOR $^{241}\text{Am}/^{148}\text{Gd}$ MIXED SOURCE	55
4.4	DETECTOR ENERGY CALIBRATION AND RESOLUTION	57
B.1	RUN ENERGY DETAILS	85
C.1	DEFLECTOR SETTINGS FOR TEST BEAMS	87

Your confusing thesis has captured my attention. Tell me more.

– Phil Hartman as Bill McNeill (Newsradio)

CHAPTER 1

INTRODUCTION

The elements making up the universe were formed during a variety of processes, beginning with Big Bang Nucleosynthesis (BBN) that formed the lightest elements. Those elements common to life on Earth were primarily formed through burning processes inside of stars, grouped together under the title of Stellar Nucleosynthesis. Depending on the conditions within the stellar environment, which are characterized by macroscopic qualities about the star (temperature, pressure, mass, etc.) and the elemental composition of the stellar interior where the burning process takes place, the reactions accessible to the nuclei within the star differ. The creation and destruction of different elements and isotopes may be inhibited or enhanced by these differing conditions, and the study of these processes at the nuclear level has spawned the field of nuclear astrophysics in order to understand the inner workings of these stars.

Within the realm of stable burning processes, changes in temperature commonly result in reaction channels or sequences becoming either energetically favorable or unfavorable.

1.1 Astrophysically-important Reaction Channels

The specific and directed study of those nuclear reactions that have an effect on the properties or life cycle of celestial bodies is grouped under the umbrella term *nuclear astrophysics*.

1.2 Beam Optics

1.3 Recoil Mass Separation

When measuring a cross section, the experimenter must make a decision as to whether to detect γ -ray particles or nuclear particles. Each of these two overarching goals carries with it their own complications and considerations, creating a variety of techniques to attempt to study the reaction in question. For some reactions of interest within the domain of low-energy nuclear astrophysics, both or these experimental directions are possible.

Gamma-ray detection suffers from background radiation producing γ rays that are picked up by the detector. This background radiation is produced by the construction materials within the laboratory in question, cosmic radiation, and the γ -ray producing reactions involving contaminants within the target material. The solutions for reducing the background from each of these sources are varied, from surrounding the detector with additional detectors to create an active shield that rejects detections that appear in both detectors within some window of time (the anti-coincidence method), to the extreme case of placing the laboratory deep underground to use hundreds of meters of the Earth's crust as a passive shield against cosmic radiation. None of the techniques, however, addresses the inherent limitation of γ -ray detection: the low efficiency of the detectors that must be used. This problem is exasperated by the extremely low cross sections common for reactions of astrophysical interest, making studies away from nuclear resonances uncommon. The other irreducible problem with these techniques is when the produced γ ray of interest is close in or the same energy as a prominent background line.

Alternatively, the produced nuclear particles may be detected instead with a high-efficiency detector. The various experimental requirements for these experiments will be discussed, along with the additional considerations that must be accounted for.

For convenience, the rest of this discussion will assume that the reaction of interest is radiative alpha capture $((\alpha, \gamma))$, where the reaction is being studied in reverse kinematics, except where otherwise noted.

St. George (Stong Gradient Electromagnetic Online Recoil separator for capture Gamma ray Experiments) is a recoil separator designed to primarily study (α, γ) reactions at low energy using stable beams provided by St. Ana (Stable beam Accelerator for Nuclear Astrophysics). The design of the separator was guided by the principles to be discussed and on the experience gained from previous recoil separators.

1.3.1 Motivation

Recoil mass separation was conceived as an alternate way to measure the cross sections of radiative capture reactions. These reactions had previously been studied by detecting the produced γ rays, subject to the limitations previously discussed. The heavy reaction product can instead be detected by a detector situated behind the target, assuming that the target is thin enough to allow the produced recoils to leave the target. In this thin target case, the incident beam will likely pass through the target as well, making it a source of background at the detector plane. In the cases of interest for nuclear astrophysics, this background count rate could be $\times 10^{15}$ that of the particles of interest and may cause damage to the detector.

The produced recoils may be filtered out from the incident beam by electromagnetic elements situated between the target and the detector. The interaction between the heavy incident beam with mass A and linear momentum p and the α particles within the target produces a heavy compound nucleus with mass $A + 4$ and momentum p . Ignoring the effect of the emitted γ ray on the momentum and assuming that there is no spread in the momentum, the use of electrostatic elements can separate the recoils from the beam based on their different magnetic and electric rigidities,

defined as

$$B\rho[\text{Tm}] = \frac{p}{q} = \frac{\sqrt{2mT}}{q}$$

and

$$E\rho[\text{MV}] = \frac{pv}{q} = \frac{2T}{q},$$

respectively, where q is the charge, T is the kinetic energy, m is the mass, and v is the velocity of the particle. With a single momentum and velocity (or kinetic energy) selected for, the recoil particles of interest can be uniquely identified by the optical system. The design of recoil separators make use of this relatively simple idea as the basis of their design. Despite this, there have been relatively few recoil separators that have been brought into service due to the complexities of their design and operation that are not adequately taken into account in this description.

1.3.2 Background Sources

A recoil separator primarily utilizes two different methods to reduce the background at the detector system: the separation of isotopes based on their rigidities to reduce the number of incident beam particles that reach the detector, and the direct detection of the heavy nuclear particles compared to the detection of the γ rays particles produced in the reaction at the target location. These reduction techniques have been briefly introduced.

Within the separator, the rejected incident beam particles (those which do not have the desired rigidities $B\rho$ and $E\rho$) are still traveling within the separator. Their final rejection and the reduction of their induced background at the detector plane must be performed by some physical element interior to the separator. A common choice of element are slits: physical barriers that stop any particle which strikes them located within the separator. The physical gap between the slits allow the desired recoil particles to pass between them while stopping the unwanted beam particles

from continuing down the separator. The location of these slits is dependent on the design and the beam optics of the separator.

While these slits stop errant beam particles, there is a possibility of those particles scattering off of the edge of the slit if the beam properties are not properly matched to the internal position or gap of the slits. These scattering events, depending on where in the separator they occur in relation to the other magnetic and electric elements and to the detector system, may allow some passage of beam particles to the detector plane and must be either rejected before that plane or taken into account in the operation of the detector system. The scattering events may also take place off of the interior of the vacuum chamber of the separator, the residual vacuum within the vacuum chamber, or diagnostic equipment installed to aide the experimenter.

The reaction also does not take place at a single energy. The incident beam invariably will have an energy spread associated with its production and will lose energy within the target before reacting with the target particles. The produced reaction products will necessarily not be mono-energetic, and additional energy spread will result from the subsequent interaction with the residual target. The reaction products also undergo either a single photon emission or a gamma cascade which will alter the reaction products' momentum vectors, adding further spread to the momentum and energy of the products that must be detected at the detector plane. Additional sources of background reduction beyond the separator must be included due to the realities of performing the experiment.

1.3.2.1 Detection System

The detector system following the separator may be used to provide this additional required beam and background suppression. Due to the separation of the recoil particles by their rigidity, a detector sensitive to both the energy and the momentum of the particles can uniquely identify those particles. There are multiple ways in

which this can be achieved, but one common design is to make use of a *time-of-flight* (TOF) detector to determine the velocity of the particles reaching the detector, and an energy-sensitive detector, measuring the total energy deposited in the detector, to provide this identification. Depending on the resolutions of the two systems, the recoils of interest can be identified by the recorded TOF and E . More importantly, those other particles that happen to reach the detector would have drastically different TOF or E or both, allowing those detections to be rejected as they did not originate from recoil particles.

The two coupled detectors would be operated in coincidence, such that those events that create a timing signal within the TOF detector must also create an energy signal in the following energy-sensitive detector in order for the event to be recorded. This operation further suppresses errant background counts at the detector system. The timing window must be matched to the properties and response of the detectors in order to ensure that the coincidence measurements from the paired detectors arise from a single particle.

1.3.3 Recoil Separators

The use of recoil separators to study radiative capture reactions has been explored recently at a number of facilities. The design of St. George is based on the knowledge gained from the design, construction, and operation of these previous recoil separator systems. The entire system, inclusive of the beam source, target, and detector, must be discussed as a whole when evaluating the capabilities of a given separator.

1.3.3.1 CalTech Separator

The design and use of recoil separators for nuclear astrophysics research was pioneered by Smith ^{*et al.*}. This separator was a proof-of-concept design to determine the feasibility of performing reaction studies with this technique.

1.3.3.2 ARES

The Astrophysics REcoil Separator (ARES) was built at Louvain-la-Neuve to study (p, γ) and (α, γ) reactions using radioactive incident beams provided by the CYCLONE44 cyclotron [1]. Self-supporting solid targets, containing the required H or He, were used for the reaction studies. The system is designed with a single magnetic dipole for momentum selection and a Wien filter for velocity selection, along with multiple magnetic quadrupoles to maintain the transportation of the to the detector system. The condensed and limited size of the separator is based on the constraints of the experimental hall [4]. The detector system consists of a single ΔEE telescope which separates out the reaction products from the remaining incident beam particles. The initial test of the separator used a stable incident beam to compare to results obtained by other methods within the lab, and the focus of the initial work was on low-lying resonances of astrophysical interest.

1.3.3.3 DRAGON

The DRAGON recoil separator at TRIUMF-ISAC was built for the same reasons as ARES, but differs in the actual construction and usage of the separator. The separator itself uses two large magnetic dipoles for momentum separation and to electric dipoles for energy selection [6]. The separator also contains steering elements within the beamline to aide in transporting the recoils to the detector plane. The extended gas target is surrounded by a large BGO gamma-ray detector for coincidence purposes

1.3.3.4 ERNA

1.3.3.5 St. GEORGE

The separator consists of six dipole magnets, eleven quadrupole magnets, and a Wien filter. The separator was designed to accept recoils with a maximum energy and angular spread of $\Delta E/E = \pm 7.5\%$ and $\Delta\theta = \pm 40$ mrad, respectively, and to provide a mass separation of $m/\Delta m = 100$ and beam suppression of a factor $\geq 10^{15}$. Combined with the HIPPO (High-Pressure Point-like target) supersonic gas jet target, St. George will be primarily used to study low energy (α, γ) reactions using stable beams.

CHAPTER 2

EXPERIMENTAL SETUP

All experimental work was performed at the Nuclear Science Laboratory (NSL) at the University of Notre Dame, using the St. Ana 5U-4 accelerator and St. George. Commissioning work for the separator began in 2014 and is currently on-going (see Section 3.3). The experiment discussed herein consisted of three separate runs, each one week long, in December 2016 and February 2017. The first run tested a proposed close location for the detection system, the second run characterized the additional magnets required for a far location for the detection system, and the third run was the primary data collection run.

The accelerator provided a high intensity proton beam to St. George for the first and third runs, and a high intensity $^4\text{He}^+$ beam for the second characterization run. The 16-strip Si detector was installed at the two proposed focal planes (F_1 and F_2 , see Fig. 2.1) to detect the produced α -particles from the $^{27}\text{Al}(p, \alpha)^{24}\text{Mg}$ reaction. Incident beam rejection was on the order of 10^9 for the first run and 10^{13} for the third run [CHECK THESE NUMBERS].

2.1 The St. Ana Accelerator and Transport Line

St. ANA (Stable beam Accelerator for Nuclear Astrophysics) is a 5 MV vertical, single-ended pelletron accelerator at the NSL, providing high-intensity stable beams to a number of experimental setups within a dedicated target room. The original designation of the accelerator by the manufacturer, National Electrostatics Corporation, was the 5U-4, denoting the five individual acceleration sections and the four

charging chains, causing the accelerator to commonly be referred to as the *5U*. Both names will be used interchangeably throughout this work.

The 5U, shown schematically in [FIGURE], accelerates a high-intensity ion beam produced by the Nanogan Pantechnik ECR source to the desired energy by energizing the terminal shell to high voltage. The acceleration tube, extending from the bottom of the shell to the bottom of the accelerator, steps that voltage down through a series of resistors and plates, creating an electric field gradient along the tube that accelerates the positively charged ion beam down and out of the accelerator. The beam is then bent around a 90° dipole magnet, called the analyzing magnet, and through a pair of vertical slits, called the analyzing slits, that provide energy identification of the beam. In addition, the current on the slits can be used as a feedback control system to regulate the voltage on the terminal shell when the accelerator is being run in “slit control mode,” providing a highly stable beam with a small energy spread. A recently performed $^{27}\text{Al}(p, \gamma)^{28}\text{Si}$ resonance scan [7] was used to determine the beam energy spread of $\sigma_{\text{beam}} \approx 0.3$ keV near a beam energy of $E_{\text{beam}} = 1320$ keV. The 5U also contains focusing, directional, and diagnostic elements used to help tune the accelerator to provide a stable and well-behaved beam.

The transport beamline directs the analyzed beam to the desired experimental area through use of focusing and directional elements: two magnetic quadrupole doublets maintain a focused beam along the beamline; the magnetic dipole switching magnet directs the beam down one of the available experimental beamlines; and magnetic steerers shift and turn the beam within the beamline. The steerers act to maintain the beam along the magnetic optical axis of the quadrupoles and maximize the amount of beam being transported down the beamline from the accelerator. Sets of diagnostic equipment are also installed at various locations along the beamline to help monitor and restrict the beam, and the entire system is kept at a high ($\approx 8 \times 10^{-8}$ torr) vacuum through use of multiple turbomolecular pumps located

along the beamline.

The final section of the transport line is between the switching magnet and the entrance to St. George. This section of beamline prepares the beam to have the required characteristics at the target location. The final magnetic steerer is used to finalize the alignment of the beam, and the magnetic quadrupole triplet creates a small, well-focused beam at the target location.

2.2 The St. George Recoil Separator

The St. George is a recoil mass separator at the NSL [5] and one of the experimental beamlines accessible to the 5U. The design and operation is based on previous recoil separators (see Sec. 1.3.3). The separator consists of six dipole magnets, eleven quadrupole magnets, and a Wien filter. The separator was designed to accept recoils with a maximum energy and angular spread of $\Delta E/E = \pm 7.5\%$ and $\Delta\theta = \pm 40$ mrad, respectively, and to provide a mass separation of $m/\Delta m = 100$ and beam suppression of a factor $\geq 10^{15}$. At lower angular spreads, the transported ions may have a larger energy spread limited by the good field region within the third quadrupole Q_3 . The design was guided by the desire to efficiently measure (α, γ) reactions with a beam mass up to $A = 40$ with high beam intensities and to fit the separator within the physical limitations of the target room at the NSL [5].

The separator is designed to transport recoils within a rigidity phase space relevant for measuring (α, γ) reaction cross sections, determined by the magnetic and electrostatic elements. The magnetic rigidity is defined as

$$B\rho \text{ [Tm]} = \frac{p}{q} = \frac{\sqrt{2mT}}{q}, \quad (2.1)$$

where p , q , m , and T are the momentum, charge state, mass, and kinetic energy of the desired particle, respectively. The magnetic rigidity defines the trajectory of

the particle's movement within a homogeneous magnetic field of strength B along a circular path with radius ρ . Similarly, the electric rigidity is defined as

$$E\rho \text{ [MV]} = \frac{pv}{q} = \frac{2T}{q} \quad (2.2)$$

with the same variable definitions as before, and defines the circular trajectory a particle takes within an electric field of strength E . The limits for these rigidities are $0.1 \leq B\rho \leq 0.45$ and $E\rho \leq 5.7$ [5].

2.2.1 Subsections of St. George

The separator is divided into three sections, based on their purpose: the charge selection stage; the mass selection stage; and the clean-up stage. The stages are separated by the focal planes. Each of these stages will be discussed in turn. The layout of St. George is shown in Fig. 2.1.

The entire separator is tuned for a single $B\rho - E\rho$ rigidity, defined by the central energy of the recoils and its mass and charge state (see Eqs. 2.1 and 2.2). For commissioning purposes, a direct incident beam was used as a “test beam” to tune the separator without having to perform a reaction. The tuned particles will then travel down the central magnetic axis of the separator. Particles that differ in energy or angle from these central particles will travel through a different path (see Fig. 3.1).

The first section is the so-called *charge selection* stage, consisting of the first quadrupole doublet (Q_1Q_2) and the first dipole doublet (B_1B_2). The doublet Q_1Q_2 focuses the recoils through the dipole pole gap, and the doublet B_1B_2 provides the first rejection of beam due to the difference in magnetic rigidity from the desired recoils. At the first focal plane F_1 , a single recoil charge state has been selected to transport through the remainder of the separator. Horizontal slits may be placed at this focal plane to aide in the rejection of incident beam particles that have undergone

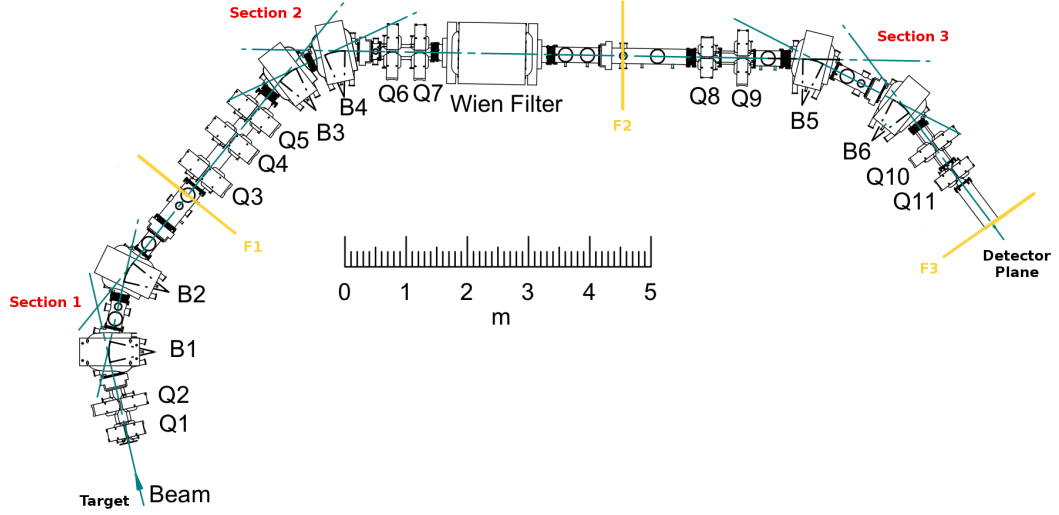


Figure 2.1. Layout of the St. George recoil separator. Quadrupoles are identified by Qn , dipoles by Bn , and focal planes by Fn . Section labels are placed near the dipole doublet within that section, and boundaries are the intervening focal planes. Adapted from Reference [5].

a charge exchange event. Slits were not used during the commissioning work or during the primary experiment. At the end of this section, both beam and recoil particles are present within the separator.

The next section is the so-called *mass selection* stage, which contains the magnetic quadrupole triplet ($Q_3Q_4Q_5$), the second magnetic dipole doublet (B_3B_4), the second magnetic quadrupole doublet (Q_6Q_7), and the Wien Filter (WF). This section's primary purpose is to reject the incident beam and create an achromatic focus at the second focal plane F_2 . This focus is horizontally narrow at the focal plane to aid in the rejection of the beam. At this focal plane, a set of horizontal slits, called the mass slits, are placed to reject the remainder of the incident beam. The focused recoil particles will pass through the center gap between the slits. The mass resolution of the separator depends on the particle distributions of the beam and recoil being focused and spatially separated at this position, and that the tail of the

beam distribution minimally overlaps with the recoil distribution.

The Wien filter operates by having crossed electric and magnetic fields, oriented such that individually they would bend a particle beam in opposite horizontal directions, as shown in Figure [FIGURE]. From the beam's perspective, the electric field bends the beam to the right while the magnetic field bends the beam to the left. The fields are provided by a pair of electrostatic plates within the vacuum chamber and a magnetic dipole outside of the chamber. A Wien filter is set to allow for a single velocity to pass through the center of the element undeflected, according to $v = E/B$. For St. George, the Wien filter provides the final mass selection for our recoils, allowing the beam particles to be filtered out from the recoil particles, since the mass difference between the two ($\Delta m = 4$ when performing (α, γ) reactions) translates into a velocity difference.

The simplified description above is not entirely accurate, since our beam and recoils exist within a phase space envelope confined by ranges of allowed positions, angles, and energies. Since we inherently have an energy distribution of our recoils deriving from the convolution of the beam energy uncertainty with the target losses of the beam and recoils and the energy change arising from the γ ray emission, we do not have a mono-energetic recoil distribution passing through the center of the WF. When taken as a whole, the elements up to and including the WF create the proper beam and recoil properties to reject the incident beam based on their mass difference.

At this point, our beam envelope can be thought of as just our *recoil* envelope, where the particles still being transported through St. George are just those recoils produced in the reaction at the target location. In reality, the envelope still contains some beam particles, either through scattering off of the interior of the beam pipe, diagnostic elements, or the residual vacuum, or through charge changing events with the residual vacuum [CITE]. Due to these factors, we cannot place the final detection

system right after the Wien filter and instead need additional elements to further reduce the background.

This final section of St. George is the so-called *clean-up* stage, where the phase space of the recoils passing through the mass slits are matched with the phase space of the detection system, providing the last rejection of the incident beam particles. This section consists of, in order, a quadrupole doublet (Q_8Q_9), the last dipole doublet (B_5B_6), and a final quadrupole doublet ($Q_{10}Q_{11}$). These magnets transport the recoil particles that passed through the mass slits at F_2 through the detection system installed at the detector focal plane F_3 . Since the detection system has a defined physical acceptance size, these magnets must reduce the physical extent of the recoil envelope within this space.

2.2.2 Diagnostic Equipment

To aide tuning the beam, additional diagnostic equipment has been developed and installed at various points along the separator. This diagnostic equipment can be divided between three basic types: Faraday cups, slits, and quartz viewers. These first two equipment types are present within other beamlines and the primary transport beamline, while the third was adapted for St. George based on principles encountered when working with other beamlines. The positions of this equipment is denoted in Figure [FIGURE].

Faraday cups are beamstops that also provide the user with the beam current being captured by the cup. The cup, shown in [FIGURE], consists of three main parts: the shield, the suppression, and the cup itself. This structure is attached to a linear motion drive, letting the cup be positioned in or out of the beam, and isolated from the beamline. The shield primarily protects the suppression from being hit by incident beam but, due to its isolation, is also a point to read out the current and determine the physical extent of the beam at that point. Ideally, all of the beam

would enter the cup portion, allowing the Faraday cup to determine the complete beam current at that location. Using the cup in this way as a tuning aide is possible since the cup locations were selected based on the beam optics properties, as those locations correspond to waist points of the beam. The suppression is necessary since electrons are emitted with energies in the rough range of $20 - 100$ eV when the beam strikes the physical cup. By biasing the suppressor to -300 eV, those electrons are directed back toward the cup, giving an accurate reading of the beam current actually hitting the cup.

Slits are an additional way to determine the passing beam current but also provide information about the spatial size of the beam. These slits are Ta plates attached to a linear motion, allowing the position to be controlled and determined from the exterior of the beamline. Each slit is isolated from the beamline, allowing the current hitting the slit to be read out at the console or to some other diagnostic program. The limiting factors for using these slits as a diagnostic device is their sensitivity, since unlike Faraday cups the slits used within St. George are not suppressed. The slits are then used as rough spatial diagnostics within the separator itself.

The quartz viewers used within St. George are divided between two types: an exterior quartz located at various exit ports, and an interior quartz that must be removed from the beamline. The locations of these camera systems are at the 0° exit ports of dipoles B_1 , B_3 , and B_5 , the end of the detector chamber, and at focal planes F_1 and F_2 . A schematic of one of the interior quartzs is shown in Figure [FIGURE]. The quartz are used for beam alignment and tuning the magnetic and electric elements of St. George, as explained in Section 3.3. When beam strikes the quartz material, the quartz fluoresces and the camera mounted immediately behind records the image and transmits it to the control console. Since this fluorescence is dependent on the beam intensity, minimum currents of 200 nA are used to ensure that the beam shape can be accurately identified. Additionally, high intensity beams can melt

the quartz material if left impinging on the system for extended periods of time, so maximum currents in the range of $1.5 - 2.5 \mu\text{A}$ were used, depending on the actual beam particle selected.

2.3 Detector System and Data Acquisition

The full St. George detector system consists of a pair of microchannel plate based time-measurement detectors and a single 16-strip Si detector for energy deposition. Combined, this detection system provides particle identification by way of the *Time of Flight vs. Total Energy* method. As residual beam particles can make it to the detector plane, either through scattering or charge exchange events, particle identification is required to provide final discrimination and beam suppression [CITERNA, DRAGON, DRS, etc]. As this experiment did not require the use of the full detection system, only the Si detector will be discussed further.

The Si detector is a Canberra PIPS (Passivated Implanted Planar Silicon) model PF-16CT-58*58-300EB, which has a detector area of $58 \times 58 \text{ mm}$ and is divided into 16 individual strips. The 16 strips allow for spatial resolution in one dimension, commonly taken to be the horizontal direction. For the experiment discussed herein, the detector was installed at focal plane F_2 . Care was taken to ensure that the quartz viewer at that same location did not interfere with the operation of the detector.

The electronics for the experiment are relatively simple, needing only the energy signals from each of the 16 strips. A Mesytec MSCF-16 shaping filter amplifier provided amplification and signal shaping following the preamplifier, and a Caen V785 32-channel multi-event peak sensing ADC transformed those signals for the data acquisition system. Power to the detector was provided by Mesytec MHV-4 high precision bias supply unit, and was biased up to $+40 \text{ V}$. Leakage current from the detector during the run was $\approx 1.4 \mu\text{A}$, but this high value was later shown to be due to the cable shielding internal to the beamline contacting the shielding installed

to protect the detector when fully retracted. During the energy calibration runs where no detector shielding was present, the leakage current was $\approx 0.3 \mu\text{A}$. The electronics used are the same as for a standard St. George experiment, allowing for an additional test of a subsystem of the full acquisition system. Data was recorded using the VM-USB crate connected to the St. George DAQ computer.

2.4 Target Chamber

A commissioning target chamber was designed and built specifically for running the commissioning experiments and solid target studies. The chamber makes use of two of the turbomolecular pumps from the Hippo target to provide a high ($\approx 7 \times 10^{-8}$ torr) vacuum at the beginning of the separator and around the target location. The commissioning chamber consists of a pair of electrostatic plates within a rotating chamber, a target ladder, and a Faraday cup. The rotating chamber allows the combined target ladder and electrostatic plates to rotate through a range of $\approx 160^\circ$ (limited by the physical space around the target location) while maintaining a high vacuum, thus the target location does not need to be vented in order to change the angle of the target ladder and plates.

The electrostatic plates can be powered up to a maximum of 10 kV each from two single-phase high voltage power supplies and are operated remotely using an Arduino-based controller. The properties of the plates (length, width, separation, etc.) were determined such that the produced electric field would be as homogeneous as possible within the limited space and provide a beam deflection of at least 40 mrad from the target location, within the physical limits of the chamber. Experimentally, deflections of 45 mrad have been achieved, allowing a full angular phase space sweep to be performed. Switching the polarity of the deflector plates must be done at the power supplies. Since the power supplies have a limited upper voltage, the maximum deflection for a test beam is limited by its electric rigidity $E\rho$. When not in use, the

current striking the deflector plates could be monitored at the control console to use as an additional beam diagnostic.

The target ladder contains a 6.35 mm diameter collimator and a 2.06 mm collimator, separated by 11.1 mm. The large collimator is primarily used for mounting self-supporting solid targets, while the smaller collimator is primarily used for beam alignment and focusing purposes. The ladder is mounted on a high precision, manually controlled linear motion drive from [COMPANY]. The ladder may be fully removed from the beamline, and the central axis is aligned with the physical location of the jet target within Hippo. A thin Al foil was mounted for the experiment described herein.

The Faraday cup following the target chamber is an isolated FN-style cup, as shown in [FIGURE]. The back of the cup can be actuated open to allow beam to pass into the separator. From extended usage of the cup, the interior connection to the rear flap had degraded to the point that when open it was electrically isolated from the rest of the cup. If actuated while beam was hitting the cup, the flap would become charged and deflect the beam entering into St. George. To counter this effect, the cup preceding the target cup was placed into the beam before the target cup was removed. Since the commissioning chamber was designed to be temporary, this cup was not repaired or replaced following this discovery.

The Faraday cup allowed for beam with a maximum deflection of > 45 mrad to enter St. George, as measured using the deflector plates. This larger angular acceptance at the beginning of the separator ensured that the diagnostic equipment did not have a detrimental affect on the experiment and based the final acceptance at F_2 to be based on the specific tune of the separator. During some tests, the deflector plates were seen to intercept some of the beam when deflecting to 45 mrad, but since this value is again larger than the designed acceptance of St. George, this was deemed to not be detrimental.

CHAPTER 3

COMMISSIONING ST. GEORGE

The St. George recoil mass separator was designed to have an energy acceptance of $\Delta E/E = \pm 7.5\%$ and an angular acceptance of $\Delta\theta = \pm 40$ mrad, based on the kinematics of a set of astrophysically important (α, γ) reactions ([5] and Section 2.2). The ion optics that maximize the acceptance of the recoil particles and the rejection and suppression of the beam particles must be experimentally determined. The calculated ion optics are related to those achieved experimentally through the measured performance of the recoil separator. By measuring the acceptance achieved through various tunes and techniques is one way to determine if the desired calculated transport properties have or have not been achieved experimentally. Recently, the energy acceptance was initially studied separately from the angular acceptance (published in [12]) to provide a relation between the predicted and experimentally determined field values. The angular acceptance was studied through a variety of methods, both in conjunction and without a corresponding energy acceptance requirement. Measuring the acceptance of a separator is paramount to using it for experimental measurements.

Two primary commissioning campaigns, determining the angular and energy acceptances for a given desired global setting of the separator, have been undertaken. The two global settings are: (i) the designed parameters for St. George for transporting heavy recoil products produced by (α, γ) reactions in inverse kinematics through the entire separator, and (ii) the altered parameters for transporting α particles produced by (p, α) reactions in forward kinematics to focal plane F_2 . From each global setting, the separator elements can be scaled based on the desired transport particle's

magnetic (Eq. 2.1) and electric (Eq. 2.2) rigidities. The experimentally determined values after scaling from the global setting may differ from the predicted scaled values when scaled over a large range, requiring multiple rigidities within the allowed rigidity phase space to be explored to fully commission the separator. For the altered forward kinematics separator settings, due to the relatively small rigidity phase space the initial test reaction covers and the fact that a direct α beam can be used, the element field strengths were directly determined prior to the data collection experiment.

For the designed inverse kinematics separator settings, various beams spanning a large region within the desired rigidity phase space were used. Test beams included light beams (^1H and ^4He) due to their ease of production and heavier beams (^{16}O and ^{20}Ne) to simulate transporting heavy reaction products through the separator. Beam particle, charge state, and energy were limited by the capabilities of the 5U to produce the desired beam. The commissioning work was divided between focusing on the energy or angular acceptance relatively independent of the other. For some of the angular acceptance measurements, a small energy spread was included to better recreate the conditions under which St. George will be used.

3.1 Theoretical and Experimental Considerations

St. George was modeled within COSY Infinity (COSY- ∞ , henceforth *COSY*), a beam optics and transport language developed at Michigan State University [10]. The initial ion optics solution for the separator was calculated by Drs. Couder and Berg at the University of Notre Dame to maximize the angular and energy acceptance for a point-like target located prior to the separator. Optimization of the individual elements' properties allowed the separator to achieve the previously-stated energy and angular acceptances, create an achromatic focus at the mass slits (focal plane F_2), and transport all recoils to the final detector focal plane F_3 (see Section 2.2). Each magnetic element is represented by a single command within the code, defining

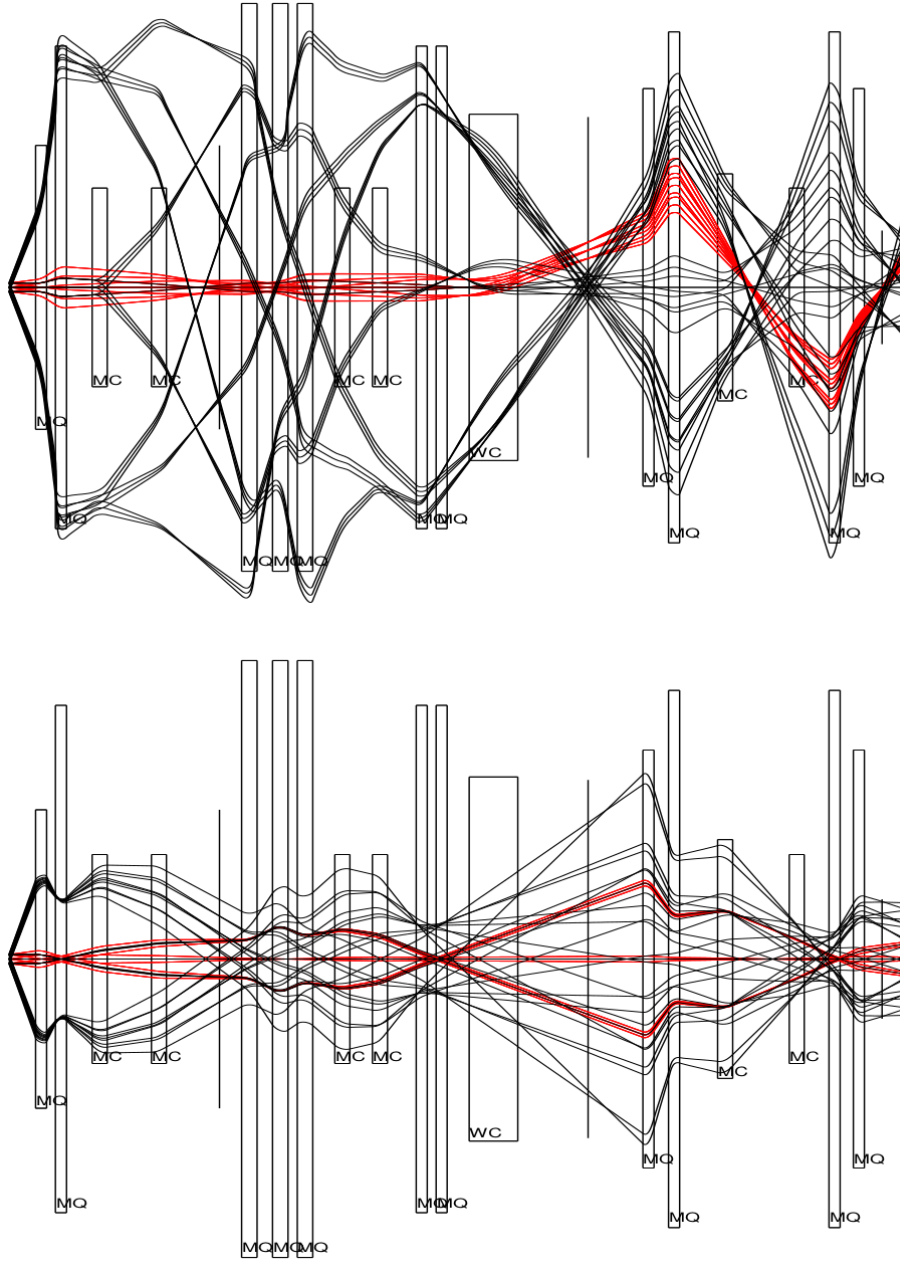


Figure 3.1. Horizontal (upper plot) and vertical (lower plot) rays through St. George. Recoil ^{41}Sc rays are shown in black and beam ^{40}Ca rays are shown in red. The beam rigidities are $B\rho = 0.331 \text{ Tm}$ and $E\rho = 2.907 \text{ MV}$, and the recoil rigidities are $B\rho = 0.331 \text{ Tm}$ and $E\rho = 2.836 \text{ MV}$. Both the beam and recoil are taken to be in the 11^+ charge state. The COSY calculation assumes that the recoil particles are spread within an acceptance range of $\Delta E/E \approx 7.5\%$ and $\Delta\theta = 40 \text{ mrad}$. The transverse scale is highly exaggerated to show detail.

the type and properties of the desired element. The three types of elements used within St. George—dipoles, quadrupoles, and the Wien filter—require different sets of values to be defined. The recoil envelope, consisting of a number of sample recoil properties used as representative rays, for the final designed configuration is shown in Fig. 3.1. For the example shown, the quadrupole pole tip fields are given in Table 4.1, where negative values represent a quadrupole focusing in the y -direction. The pole tip fields for (α, γ) experiments are for the test particles shown, while those for (p, γ) experiments are specific to this work (see Section [REFERENCE]). The actual fields used will depend on the rigidity of the desired particle to transport through the separator and can be scaled from these values.

The initial ion optics solution creates a transport map for particles passing through the entire separator that can be analyzed independently of the ray traces and provide the mathematical backing to the particles' trajectories within St. George. The transport map is dependent on the quantities

$$\begin{aligned}
r_1 &= x & r_2 &= a = p_x/p_0 \\
r_3 &= y & r_4 &= b = p_y/p_0 \\
r_5 &= l = -(t - t_0)v_0\gamma/(1 + \gamma) & r_6 &= \delta_K = (K - K_0)/K_0 \\
r_7 &= \delta_m = (m - m_0)/m_0 & r_8 &= \delta_z = (z - z_0)/z_0,
\end{aligned} \tag{3.1}$$

where a and b are analogous to angles within each plane, δ_K is the energy difference from the desired energy K_0 , δ_m is the mass difference from the desired mass m_0 , and δ_z is the charge from the desired charge state z_0 [10]. The desired quantities are the values used to calculate the magnetic (Eq. 2.1) and electric (Eq. 2.2) rigidity, and thus set the fields of the elements within St. George, of the particle to be transported through the entirety of the separator. The time of flight difference l is not considered in analyzing the separator. The transport map contains terms up to fourth order.

The original ion optics calculation used default parameters to describe the fringe fields of the optical elements. A change in the shape of the fringe field can change the trajectory of the particles within the separator, as the total field that the particle interacts with changes in magnitude. Since the fringe fields used to find the ion optics solution and those created by the actual magnetic elements within St. George may be different, the required field strength may also be different. The pole tip fields for a given particle rigidity, determined by the current setpoint for that magnetic, must be found experimentally, or a new ion optics solution using fringe field parameterizations that more accurately reflect those exhibited by the magnetic elements must be found. The procedures for each of the three different types of elements necessarily differ based on what diagnostic equipment is available.

The magnetic settings for the dipole magnets, determined by the rigidity of the particles, can be determined by observing the trajectory of the particles within the separator, where trajectories close to the central axis are desired. As this trajectory can be directly observed using diagnostic equipment aligned with the axis, it is relatively easy for the required values to be found within some confidence interval around the theoretically desired value. Once these coarse values are found, the final values which direct the particle beam along the magnetic optical axis of the following quadrupoles can be determined by minimizing the off-axis steering effects of the quadrupoles by adjusting the dipoles' magnetic fields within a small window of values.

Setting the Wien filter can be done in a similar manner. The electric field strength is determined from the analyzed energy of the particle, the known charge state, and the desired bending radius of the filter. Thus, the electric field strength can be set to an exact value, requiring the magnetic field to be set to match the properties of the electric field. The strength of the magnetic field is set such that the bending radii of the two fields are the same and so that the particle beam continues along the

magnetic optical axis in the same manner as described previously with the standard dipoles. The Wien filter was designed with magnetic yokes at the entrance and exit of the filter to restrict the magnetic fringe field so that it matches the electric fringe field created by the electrostatic plates, and those must be adjusted to their proper positions before the magnetic field can be set.

The magnetic quadrupoles, due to the inability to directly observe the trajectory of the focused particles within the separator at all possible angles and energies concurrently to achieve the required acceptance properties of the separator, require a similarly complicated and restrictive procedure to determine the experimental settings that match the results of the beam optics calculations. The full procedure is outlined in 3.3.1.2.

3.2 Separator Properties

The elements, power supplies, and supports were provided by Bruker Biospin and installed in 200X. The separator design requirements for the strengths of the optical elements were based on the maximum beam energy of the older KN single-ended Van de Graff accelerator and the possible charge states produced by its internal ion source. The 5U and ion source have similar properties to this system. The power supplies for the magnets provide highly stable direct currents for each magnet individually, with $dI/I \approx 10^{-4}$ for the quadrupoles and $dI/I \approx 10^{-5}$ for the dipoles. The upper current limit is different for each magnet. The separator uses a robust water cooling system able to maintain the required 80 ± 2 °F magnet temperature for the entire system. The system is able to maintain the temperature even when all magnets are at their maximum currents for extended periods of time.

The Wien filter electrode power supplies are set separately based on their voltage, with voltage stability $dV/V \approx 10^{-5}$ in the range commonly used for experiments. The upper limits for these power supplies are ± 110 kV, with voltages below ≈ 70 kV

used during previous work. The stability of the voltage is dependent on prior conditions within the vacuum chamber, requiring conditioning of the plates before higher voltages can be achieved. For voltages above ≈ 50 kV, the plates were conditioned to voltages at least 10 kV above the desired setpoint to provide a stable running condition. For lower voltages, no conditioning is necessary unless the vacuum chamber was recently vented (exposed to atmospheric pressure gases).

The properties (entrance and exit apertures, length, maximum field strength, good field region, etc.) were determined within the ion optics solution to transport the desired recoils, and built to match those specifications. The entrance and exit pole faces for the dipoles were designed to provide higher order corrections to the particle trajectory, since additional higher order magnets could not be used [5]. Additionally, the shape of the Wien filter electrostatic plates were designed such that the electric and magnetic fringe fields were closely matched.

3.2.1 Magnetic Fringe Fields and Effective Field Lengths

Detailed two-dimensional magnetic field maps for multiple excitations of each magnet were provided by Bruker. The field maps allow a check on the good field region for each magnet and provide a description of the fringe fields. Field strengths at each location are measured in mT. The fringe fields for each magnet, excitation, and measurement radial distance can be analyzed separately if desired. From this data, the shape of the fringe field and the effective field length of the magnetic elements can be determined. As these values are essential to setting the necessary values for the quadrupoles, the analysis of the field maps focused on these elements.

A single edge fringe field is described by the Enge function given by

$$E(z) \equiv \frac{1}{1 + \exp \left[\sum_{i=0}^{N-1} a_i \left(\frac{-z}{D} \right)^i \right]}, \quad (3.2)$$

where a_i are the desired expansion coefficients, D is the aperture diameter, and z is the longitudinal distance [2]. The formulation above is used within COSY to describe user-defined fringe fields. For a short magnet, which the St. George quadrupoles can be considered to be, the entrance and exit fringe fields are not completely independent of each other, since the fringe fields extend into the central region of the magnet. Instead of fitting each fringe field separately, we can instead fit the entirety of the magnetic field profile using a combined “short” quadrupole function, in terms of the Enge function, given by

$$k(z) = k_0 [E(L/2 + z) + E(L/2 - z) - 1], \quad (3.3)$$

where k_0 is a scaling parameter for the central field and L is the effective field length [2]. This formulation assumes a symmetric field profile, as both the entrance and exit fringe fields are modeled with the same Enge function. The effective field length, defined as

$$L = \frac{1}{B_0} \int_{-\infty}^{\infty} B(z) dz, \quad (3.4)$$

where B_0 is the field strength at the center of the magnet, is the field length if the field were described with a pure “hard edge” or Heavyside function at the entrance and exit, i.e. no fringe fields.

Using the field maps provided by Bruker, we can determine the Enge coefficients and the effective field lengths for our magnets. For all calculations, since the field near the center of the magnet is relatively weak, the fields within 2 cm in the radial direction of the central axis were not used for determining either the effective field length or the Enge coefficients. Additionally, the effective field length and the shape of the fringe field were assumed to not differ with different magnet excitations, so all available data were used for each magnet at the same time. An example using Q_{10} of the normalized fields used and the resulting fit is shown in Fig. 3.2.

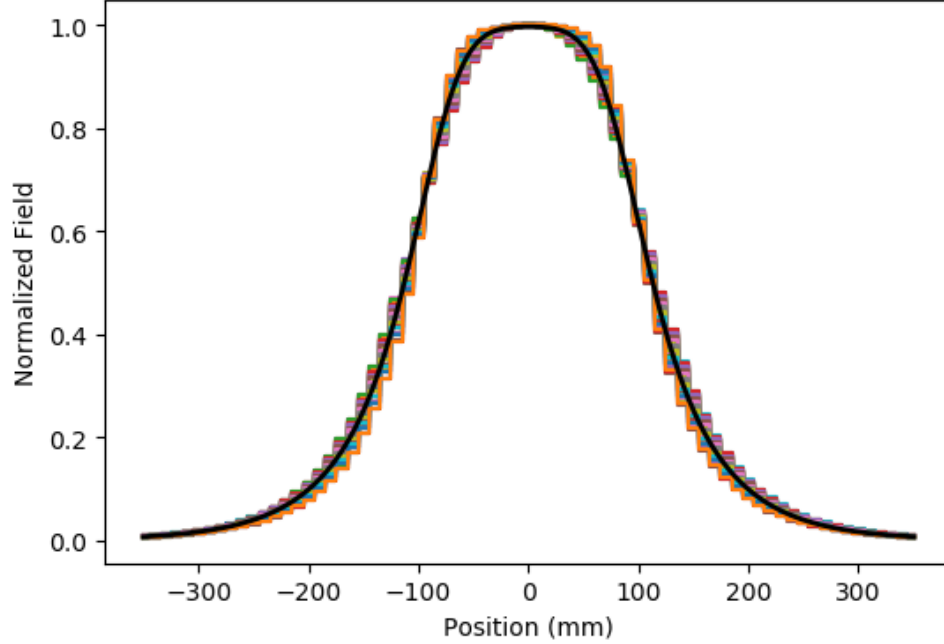


Figure 3.2. Normalized field and the resultant fit to the fringe field for the example quadrupole Q_{10} . The parameters of the fit are given in Table 3.1.

The effective field lengths were calculated directly from the field maps by integrating along the z -direction for each radial distance provided. Since the maximum field strength for a given magnet current varies depending on the distance from the center, the individual “traces” of the magnetic field along the z -axis were normalized. This normalization is shown in Eq. 3.4 as the constant factor outside of the integral. The integration was performed using the Simpson’s Rule routine provided by the SciPy Python package [8]. An average of these lengths was used. Differences between the calculated effective field length and those used within the initial ion optics solution were within 2 %. The new effective field lengths were used for all subsequent calculations.

Using the same normalized field “traces” along the z -axis, the Enge coefficients describing the shape of the fringe field may be determined. The field profiles at each

TABLE 3.1

ENGE COEFFICIENTS FOR Q_{10} COMPARED TO COSY DEFAULTS

Coefficient	Q_{10} Values	COSY Defaults
k_0	0.997 314 89	
a_0	0.372 552 61	0.296 471
a_1	6.186 997 78	4.533 219
a_2	-5.555 141 15	-2.270 982
a_3	6.962 108 51	1.068 627
a_4	-4.825 813 28	-0.036 391
a_5	1.313 578 7	0.022 261

radial distance were fit simultaneously. Using the default Enge coefficients as the initial parameter guesses, the summed mean squared error between the data and Eq. 3.3 was minimized using the Nelder-Mead downhill simplex minimization (see [14]) provided by SciPy. The additional factor k_0 was included in the fit, but is not needed when defining a fringe field within COSY. The process was repeated for each quadrupole separately. The updated Enge coefficients and their comparison to the default values used by COSY for Q_{10} can be seen in Table 3.1, and the difference in the shape of the fringe field can be seen in Fig. 3.3.

In some cases, the field maps were not recorded far enough away from the center of the magnet for the fitting routine to converge, primarily due to the field not adequately reaching zero. In those cases, “dummy” points of zero field were pre- and post-pended to the individual “traces” at distances greater than 5 m from the center of the magnet to aide in convergence.

The default COSY coefficients for the fringe field were compared against the data

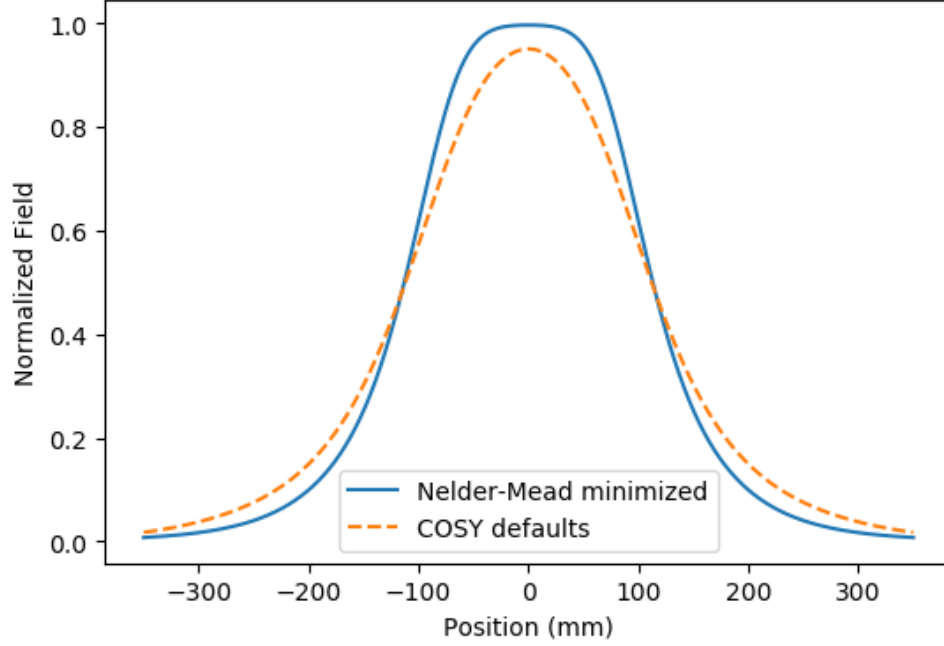


Figure 3.3. Comparison between fringe fields for the example quadrupole Q_{10} . The COSY default parameterization for the fringe field is the dashed orange line, and the fitted fringe field is the solid blue line. The distinct difference between the two field characterization requires the higher order effects arising from the fringe field to be taken into account.

and shown to not adequately describe the field maps. The summed mean squared error when using the short quadrupole formalization and the default COSY parameters was significantly larger than that found through the minimization routine, and the difference was shown to be statistically significant. A visual comparison between the two models for Q_{10} is shown in Fig. 3.3.

3.3 Energy and Angular Acceptance

The energy and angular acceptances of St. George were determined experimentally through a series of experimental campaigns using multiple rigidities. The energy acceptance without a corresponding angular acceptance was shown to ex-

ceed the designed acceptance at zero degrees, with a measured energy acceptance of $\Delta E/E = \pm 8\%$ for ten different beam rigidities covering the phase space region for astrophysically important recoils [12]. The angular acceptance has been shown to meet the desired $\Delta\theta = \pm 40$ mrad in limited cases with an energy spread of $\Delta E/E = \pm 3\%$. The full total acceptance has not yet been measured within the designed phase space limits of St. George, with work ongoing.

Within the following discussion, the term “test beam” will be used in reference to an incident beam produced by the 5U with a desired rigidity. These test beams are defined by the beam particle, energy, and charge state selected by the operator and produced by the 5U. These beams were chosen for to provide particles with the desired rigidity and with beam currents in the range of $0.5 - 3 \mu\text{A}$ in order for the diagnostic equipment to properly measure the beam. Additionally, those beams that commonly had highly stable 5U and ion source running conditions over extended times were selected to reduce beam preparation steps by the operators.

Acceptance measurements first probed the energy acceptance within the designed $B\rho - E\rho$ phase space. The rigidity phase space limits, along with measured acceptances and ranges for proposed future experiments is shown in Figure 3.4. While it is not possible to produce test beams with the 5U that completely span this phase space, the regions of astrophysical interest are accessible, and work focused on this region.

3.3.1 Beam Tuning and Properties

The commissioning runs followed a similar procedure for beam preparation using the 5U and the transport line. The beam rigidities were chosen to cover a region within the phase space limits of the separator that cover recoils produced through reactions of astrophysical interest. Both light (^1H and ^4He) and heavier (^{16}O and ^{20}Ne) beams were used to probe different regions of that phase space. Angular acceptance

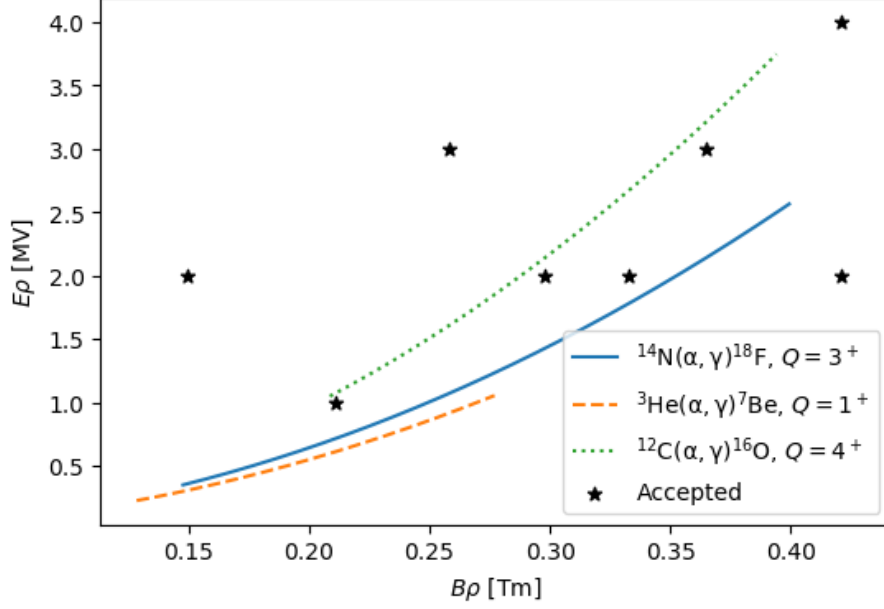


Figure 3.4. Designed $B\rho - E\rho$ rigidity phase space for St. George. Stars represent rigidities that have been shown to have the full $\Delta E/E = 8\%$ energy acceptance. Reactions shown are probable first experiments using St. George that use beam energies accessible with the 5U: ^{14}N at $E_{\text{beam}} \approx 0.7 - 5.0$ MeV (solid blue line), ^3He at $E_{\text{beam}} \approx 0.25 - 1.2$ MeV (dashed orange line), and ^{12}C at $E_{\text{beam}} \approx 3.0 - 10.0$ MeV (dotted green line). These energy ranges cover some of the astrophysically important ranges for the given reactions. Adapted from [12].

runs to date have only used lighter beams. The energy uncertainty of the beam is approximately 0.3 keV (see Section 2.1), and a conservative value of 0.5 keV will be used when necessary.

Beam preparation can be divided into two segments: preparing the $\Delta E = 0$ test beam to enter into St. George along the central magnetic optical axis, and transporting that beam along the central magnetic optical axis within St. George. The following procedures were used for all acceptance measurements, with differences being minor. The diagnostic equipment described in Section 2.2.2 was essential to performing the beam preparation steps and their use is highlighted below.

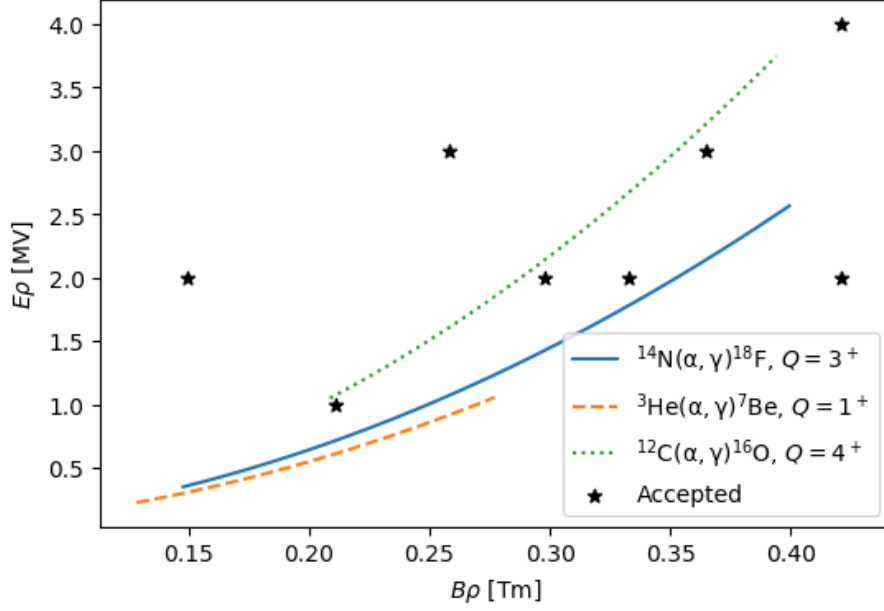


Figure 3.5.

3.3.1.1 Before St. George

The test beam must meet simple requirements in order to be useful for commissioning St. George: it must enter St. George along the optical magnetic axis, and it must have a narrow waist point with a circular cross section at the target location. Additional requirements were shown to be beneficial experimentally: the focus must not be highly divergent, and the accelerator must be providing highly stable beam current with low energy uncertainty. The divergence of the beam was roughly known based on the focusing strength of the preceding quadrupole magnets required to provide the desired beam properties at the target location, with higher focusing strengths resulting in a more divergent beam. A rough sketch of this relation is shown in Figure 3.5.

The beam intensity is dependent on which diagnostic equipment will primarily be used. The isolated Faraday cups cannot read current below 50 enA when read through

the logarithmic amplifier at the console, and the current can't be above 20-30 $e\mu\text{A}$ as the cups are not currently water cooled and a high intensity and focused beam may melt some of the components. This upper current limit was not approached during the tests, since the cups were used in tandem with the quartz viewers. The quartz viewers are limited to beam currents of a maximum of 3-5 $e\mu\text{A}$, as higher currents risk heating up the quartz to a high enough temperature to cause them to shatter or melt. Since four of the quartzes are also barriers between the high (10^{-8} torr) vacuum within St. George and atmosphere, this limit must be carefully avoided. In practice, currents between 500 nA and 4 μA were used, based on the exact properties of the ion source for that particular run, the beam species, and the locations of slits on the primary transport line used to reduce the beam current.

The procedure for aligning the test beam to the magnetic optical axis is described below. Major subsections of the procedure will begin with a short title in bold to guide the reader. The elements on the main transport line that may be necessary to adjust are the switching magnet with the X_6 steerer, and the Y_5 and Y_6 steerers (locations shown in Figure [FIGURE]). The steerers are labeled as such based on their position along the main transport line. Steerers X_6 and Y_6 are part of the same physical steerer but can be operated independently. Additionally, the quadrupole triplet directly before the target location will be necessary for final tuning.

Aligning the beam to St. George's optical axis: The desired test beam is transported down the St. George transport line and monitored with the Faraday cup at the target location, called the *target cup* for beam current stability. Diagnostic equipment before the target location are used as an aide to transport the beam and ensure that it has the desired properties. If necessary, the beam current is reduced. The quadrupole triplet is not be used at this point, since the beam may not be entering the element along its magnetic optical axis.

The beam is sent into St. George. With no field in Q_1 , Q_2 , and B_1 , the beam hits

the quartz viewer at the 0° exit port of the magnetic vacuum chamber, called the B_1 *quartz*. If the beam does not strike the quartz, then the final set of steering elements needs to be adjusted to send the beam into the quartz. When using the angular deflection commissioning chamber, the current readbacks from the plates provides an additional diagnostic on the trajectory of the beam.

Checking for steering: Quadrupoles Q_1 and Q_2 are adjusted independently of each other, and the resulting motion of the beam on the quartz is recorded. If the beam is aligned with the central magnetic optical axis of either quartz, the quadrupole will only focus the beam and not shift its position on the quartz, i.e. the spread in the beam will change but not its central position. The two quadrupoles must be adjusted independently of each other as any induced steering from a beam misalignment in one may be counteracted by a misalignment in the other quadrupole. If the beam is steered by either quadrupole, the steering elements corresponding the the focus direction of the offending quadrupole (Y_5 and Y_6 for Q_1 , the switching magnet and X_6 for Q_2) are adjusted to reduce the amount of steering by that quadrupole.

A quadrupole steers a beam when the beam enters the magnetic element misaligned with the optical magnetic axis. Assuming that the element is brought from zero to defined strength, the focal length of the quadropule changes from ∞ to a length f . The effect on the beam is that those regions of the beam away from the optical axis are brought to pass through this focal point. When a beam is aligned with the optical axis, there is an equal amount of the beam on either side of this optical axis, so the beam spot will narrow along the focusing axis of the quadrupole. The beam will also extend along the other axis. If the beam is not aligned with the optical axis, this beam motion to the focal point will be viewed as a lateral motion along the focusing axis of the quadrupole. A sketch of this effect can be seen in Figure 3.6.

The goal for adjusting the steering elements before St. George is to have each

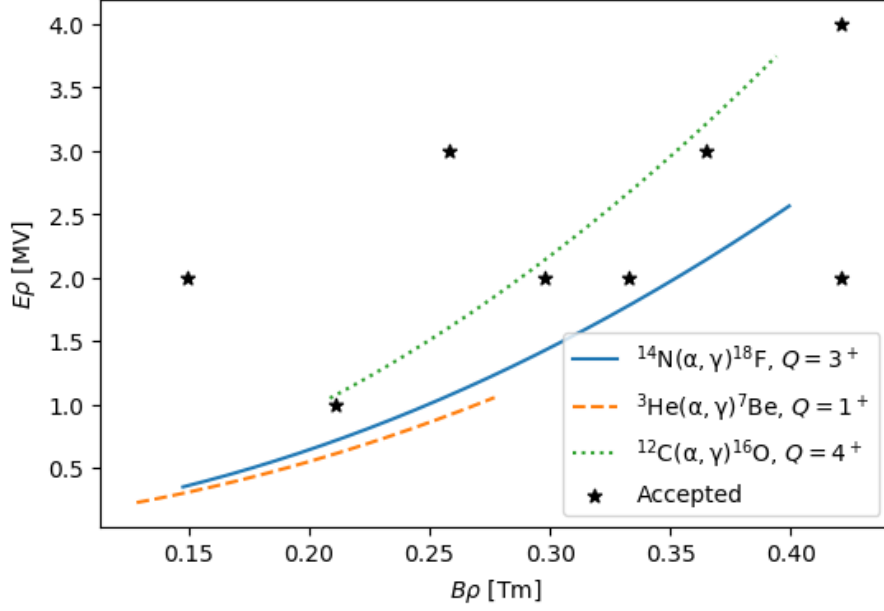


Figure 3.6.

quadrupole induce no steering on the beam. In practice, each change to the steering elements either increases or decreases the amount of steering in the direction of that element. The crossover point, where the beam switches from steering left to steering right for example, can be used to restrict the possible phase space of steerer values, as the beam must have a zero deflection position between those two extremes.

While each direction should be independent of each other, if the beam is far from the magnetic optical axis, a single quad may induce steering in both directions. When minimizing steering in a single direction, say the x -direction, the other direction must also be checked frequently.

At the end of this process, the beam is not deflected when the field strength for either Q_1 or Q_2 is increased or decreased independently of the other quadrupole. The beam may be said to be entering St. George along the optical magnetic axis. Due to the short distance between the first quadrupole doublet and the B_1 quartz, it may be necessary to increase the sensitivity of the steering to ensure that we are as aligned

as possible to the axis.

Increase sensitivity: The beam is then sent further into St. George, first to the B_2 quartz located within the beamline then the B_3 quartz. The steering of Q_1Q_2 is again checked in the same fashion as before. As these quartzes are located further from the quadrupoles, they give a higher sensitivity to steering affects from misalignment than just using the B_1 quartz at the trade-off that the the quadrupoles can only be set to lower field strengths. Since the quartz is further from the focusing elements, the same focusing strength will create a larger beam spot on the quartz viewer. This effect can be seen in Figure 3.6.

These additional checks require B_1B_2 to have field. While these two dipoles must have an exact field strength when performing acceptance measurements or an experiment, at this point their fields only need to be coarsely set such that the beam strikes the desired quartz. While the higher order corrections from these magnets do play a role in the direction and focusing of the beam, that contribution has no effect on determining beam alignment within the quadrupoles.

The steering elements are adjusted in the same fashion to minimize steering in Q_1Q_2 . Since this steering was minimized during the previous step, these adjustments should be minimal. It may be necessary to have a weak field in B_3 in order to see the beam on the B_3 quartz, due to possible machining misalignments of the port that the quartz is attached to and the residual magnetic field within the dipole.

Include the quadrupole triplet: As the last focusing element before St. George, the quadrupole triplet (henceforth simply the *triplet*) is the final adjustable element to determine the beam properties when entering the separator. The triplet is used to focus the beam to a small spot at the target location, a requirement for both experiments and acceptance measurements. As it and Q_1Q_2 should lie on the same magnetic optical axis, its steering must also be checked and minimized if its use is desired for the present experiment. It was not used in all cases as the coarse target

focus provided by the previous quadrupole doublets on the main transport line were deemed sufficient.

Before moving the beam off of the B_1 quartz, the steering effects of the triplet must be characterized in the same fashion as Q_1Q_2 . During the steering minimization steps, both the triplet and Q_1Q_2 must both be minimally steering before moving forward.

Due to minor misalignments between the triplet and Q_1Q_2 , it is usually not possible to have all elements nonsteering at the same time. In these cases, the steering of Q_1Q_2 should take precedence while having the triplet minimally steering. While the steering of the beam prior to the target location is important, experimentally the steering of the individual elements within the triplet cancel or nearly cancel each other out when the triplet is minimally steering, reducing that problem.

At this point, the main transport line has been tuned to prepare a well-focused and well-aligned beam entering into St. George. These elements are not to be touched during the rest of the tuning process. The triplet, due to the possibility of it having minor steering effects, must also have zero field for the remainder of the steering checks, and will be turned on for the actual measurement.

3.3.1.2 Within St. George

Once the test beam has been aligned to enter the separator along the magnetic optical axis, it must also be aligned to the magnetic optical axes of all of the quadrupoles within the separator. This alignment is done using only the dipoles B_{1-6} and the WF. Any minor misalignment in the vertical direction should have been corrected during the previous steps, but there is the possibility that there will be vertical steering within the separator, both from that misalignment and effects from the dipoles and quadrupoles. Within St. George, this equates to the y -focusing quadrupoles ($Q_{1,4,7,8,11}$) potentially steering minorly in the vertical direction despite the best ef-

forts of the operator. As there are no elements within St. George that could correct for this, the steering effect of these quadrupoles may not be able to be eliminated. The procedure for this second alignment is straightforward, as the only elements used to adjust the steering of the quadrupoles are the two dipoles immediately prior.

Tuning to the WF: With the beam striking the B_3 quartz, quadrupoles Q_{3-5} are checked for steering. The primary focus of these steering checks will be on Q_3 and Q_5 which focus in the horizontal plane. The magnetic fields within B_1B_2 are adjusted to make these quadrupoles non-steering or minimally steering. The field precision is on the order of 0.1 G, read back by the Hall probes.

Due to potentially small misalignments in the St. George quadrupoles in relation to each other, it is commonly not possible to have Q_{1-5} non-steering simultaneously (see [12]). In these cases, minimal steering can be achieved through Q_{3-5} when Q_1Q_2 are non-steering by adjusting B_1B_2 . At this point, dipoles B_1B_2 are set to the value corresponding to the magnetic rigidity of the particle and to maintain the test beam alignment to the optical axis.

Dipoles B_3B_4 are brought up to their rough field value to send the beam through the WF and onto either the WF quartz or the B_5 quartz. The quadrupoles Q_{6-9} are checked for steering, adjusting B_3B_4 to minimize the steering. Since there is some residual magnetic field within the Wien filter, the electric field is brought up to compensate for this bending to keep the test beam along the optical axis through Q_8Q_9 . The field required is calculated by determining the bending radius caused by the residual magnetic field and creating the equivalent bending radius in the opposite direction for the particle's $E\rho$.

As the beam envelope has expanded, it will be necessary to bring Q_{1-5} to their desired values in order to check the steering of the remaining quadrupoles. Since these quadrupoles have been shown to be minimally steering, their effect on the beam trajectory through remainder of St. George should be negligible. It may be

necessary to have a weak field in B_5 in order to see the beam on the B_5 quartz for the same reasons as explained previously for B_3 .

Setting the WF: For a test beam with $\Delta E = 0$ and $\Delta\theta = 0$, the elements within St. George will be set to transport this along the central axis based on the test beam's rigidity. Since the energy of the beam is well known and the charge of the beam is exact, the electric rigidity $E\rho$ is also well known. The electric dipole within the WF is set for this rigidity and held constant for the remainder of the tuning process.

The magnetic field is set similarly to the other dipoles: to minimize the steering induced by the next set of quadrupoles (Q_8Q_9). Since the test beam was aligned to the optical magnetic axes of this quadrupole doublet in the previous step, the WF magnetic dipole must return the beam to this orientation. Additionally, since the elements within St. George act to prepare the beam to be separated by mass by the WF, the quadrupoles Q_{1-7} must be set to the values determined by the test beam's magnetic rigidity $B\rho$.

The magnetic field for the WF is read back using a Hall probe located on the pole face. The field can be set precisely and related to the fields in the other dipoles. Once the magnetic field is set such that Q_8Q_9 do not steer the beam, the full WF is set.

Tuning through the detector chamber: Dipoles B_5B_6 are set to their rough values based on the $B\rho$ of the test beam, sending the beam through the detector chamber and onto the last quartz, called the *detector quartz*. As before, due to the size and shape of the beam envelope, Q_8Q_9 must be set to the required values. The final two quadrupoles $Q_{10}Q_{11}$ are checked for steering, and B_5B_6 are adjusted to minimize that steering.

Since the test beam is traveling through the detector chamber, the entire detection system must be pulled out of the way of the beam. Magnetic shields have been placed below the MCP constructs to remove the effect of the magnetic fringe fields on the

beam deflection [13]. Once $Q_{10}Q_{11}$ are non-steering, the test beam is fully aligned to the optical magnetic axis of St. George.

3.3.1.3 Collimator and Target Position

The 2 mm diameter collimator at the target location (see Section 2.4) is used for setting the triplet to the proper values. A narrow waist beam at the target location is a requirement to achieve the maximum angular and energy acceptance for St. George. With the collimator in place, the triplet is adjusted such that the beam transmission, defined as the ratio between the beam currents before and after the collimator as read by two separate Faraday cups, is maximized and ideally close to 100 %.

Since the target chamber may rotate around its central axis, it is possible for the location of the collimator to become slightly misaligned between runs. Additionally, the triplet may induce some minor steering at the target location, potentially moving the focal point radially from the optical magnetic axis. The target collimator position is then not a fixed value but must also be tuned to maximize transmission. Once the collimator position is found, the target position is immediately known.

Rotation angles between -5° and $+25^\circ$, where 0° is to the right from the beam's perspective, and extensions of 91 – 96 mm of the mounted linear motion have been explored. Maximum transmission has been found for collimator positions within this range of rotation angles and extension distances for multiple beams, restricting the total possible search space for the collimator. Extensions of the target ladder of ≈ 94 mm, and rotation angles near $+10^\circ$ are common “best positions” for the collimator.

For acceptance measurements, the collimator is used to create a focal point at the target location. Once the beam preparation is complete, it is retracted from the beamline. When a target is used as a degrader, the collimator position is used to determine the target position.

3.3.2 Energy Acceptance

The energy acceptance of St. George at $\Delta\theta = 0$ mrad was measured to be $\Delta E/e = \pm 8\%$ for ten different rigidities (see Fig. 3.4 and [12]). The measurements took place before the capability to measure the angular acceptance and will be remeasured as part of a total acceptance measurement campaign. Test beam rigidities were chosen to cover an adequate region within the designed phase space near the rigidities expected for recoils of astrophysical interest and based on the restrictions imposed by the 5U and ion source.

For a given set of field settings for a test beam at $\Delta E = 0$ that provide 100% transmission between the target cup and a Faraday cup located within the detector chamber at focal plane F_3 , the separator is said to accept an energy difference if the test beam is changed to that different energy and still have 100% transmission between those two cups. To state that St. George has an energy acceptance of $\Delta E/E = \pm 8\%$, a single set of fields for the elements within the separator transmitted 100% of the test beam between the two cups when its energy was changed within that energy change.

The procedure for measuring the energy acceptance of a single rigidity is outlined below. The slits located at the post-WF focal plane F_2 were used to define a beam center. As the tune for a given recoil is supposed to be achromatic at this location, these slits were used as both a diagnostic on the path of the beam and a check of this requirement during the measurements. Note that the tuning process for these measurements did not make use of the in-beam quartz viewers at F_1 and F_2 since they had not yet been installed.

Initial setup: After tuning a beam along the optical magnetic axis as described in 3.3.1, all elements within St. George are at a given field. The dipole elements, including the WF, are not touched. The transmission between the target cup and the F_3 cup is measured. If the transmission is 100%, the beam energy was changed.

If not, then the quadrupoles were retuned to transmit 100 % of the test beam between the two cups.

Quadrupole retuning was done systematically to prevent over- or under-focusing the beam at any location within St. George. With the beam on the F_3 cup, each quadrupole was adjusted individually to determine what field is required to transmit 100 % of the beam to the cup. After finding that field, the difference is recorded and the quadrupole is returned to its original value. This process is repeated for every quadrupole acting independently. If a single quadrupole could not achieve 100 % transmission on its own, it was not included in the next step. Assuming N quadrupoles adjusted by ΔB_i to give 100 % transmission, the individual quadrupoles Q_i were changed by $\Delta B_i/N$. This approach usually resulted in achieving 100 % transmission for the $\Delta E = 0$ case.

The quadrupole adjustment described was used at every step if the tune was shown to not transmit 100 % of the test beam. Previous settings of the quadrupoles were recorded to map regions of field strengths where 100 % transmission was achieved for different energy changes.

Changing energy: The beam energy was changed to $\Delta E/E = -8\%$ by changing the accelerator. The transport beamline was scaled automatically to account for the change in rigidity. The beam was shown to enter into St. George along the optical magnetic axis by putting the fields within Q_1 , Q_2 , and B_1 to zero and checking the steering of the first two quadrupoles. Since this energy change is minor, in most cases only the switching magnet needed to be changed. The magnets $Q_1Q_2B_1$ were brought back to their required values and transmission between the two cups was checked.

If the beam was fully transmitted to the F_3 cup, the settings for St. George were said to have an energy acceptance of $\Delta E/E = -8\%$. The beam energy was then changed to $\Delta E/E = +8\%$, following the same procedure, and transmission was

checked. If the beam also was fully transmitted, the separator tune was said to have an energy acceptance of $\Delta E/E = \pm 8\%$ and the measurement was complete.

Where 100% transmission was not achieved, the quadrupole scaling described previously was used. The new tune was recorded, and the beam energy was returned to $\Delta E = 0$ to check transmission. This process was continued until all three energy points had 100% transmission for a single setting of St. George. During this cycling, referring to previous values was used to prevent correcting the tune in one direction at one energy only to change back to the previous tune at another energy.

Since the F_2 slits were placed around the beam center, achieving 100% transmission was only possible if test beam had a nearly or completely achromatic focus following the WF, one of the requirements for normal operation of the separator.

Additional measurements: For subsequent energy acceptance measurements, instead of using the COSY predicted values, an energy acceptance tune scaled based on the magnetic rigidity $B\rho$ of the new test beam was used for the initial quadrupole settings. If the difference in $B\rho$ was sufficiently small, the required adjustments to the quadrupole fields were minimal, speeding up the measurement process. As more individual energy acceptance measurements were made, the scaling based on $B\rho$ became more robust to slight differences in beam preparation and species.

Once the ten rigidities within the astrophysically interesting phase space of the separator were measured, work moved to measuring the angular acceptance.

3.3.3 Angular Acceptance

As of this writing, the angular acceptance of St. George has been measured to be $\Delta\theta = \pm 40$ mrad in the horizontal and vertical planes for a single rigidity. The acceptance was shown by ensuring 100% transmission when deflecting the beam 40 mrad in each direction, and quadrupole adjustments followed the same procedure as during the energy acceptance measurements. The measurement was done without

a corresponding energy acceptance, and without the requirement that the test beam be focused at the focal plane F_2 following the WF and without the beam passing through the slit opening at that location for all deflection angles. The measurement was then a single “proof of concept” that an angular acceptance could be measured using the new diagnostic and control equipment installed. Due to complications with the measurement process, multiple attempts at measuring the angular acceptance, each with a different procedure, were tried. These attempts are outlined below.

Deflector plates only: A test beam is tuned to provide a non-steering beam with 100 % transmission between the target and F_3 cups. The deflector plates (see Section 2.4) are rotated so that they deflect the beam in a single plane. The horizontal plane was commonly chosen first. Since the entrance aperture for the target cup is larger than 40 mrad, it does not intercept any of the beam when it is deflected. Angles between 0 and 40 mrad were used and the current on the F_3 cup was monitored. The maximum angle that provided 100 % transmission was recorded.

If the maximum angle achieved was not 40 mrad, the quadrupoles were tuned in the same fashion as for the energy acceptance measurement but with the deflector plate set to an angle greater than was accepted such that the beam is still partially captured by the cup. The changes to the quadrupole fields were recorded, and all quadrupoles that could provide 100 % transmission were scaled to new values. The beam was returned to $\Delta\theta = 0$ to ensure that the new tune still provided 100 % transmission in this case, and the deflection was changed.

A single plane was checked for ± 40 mrad first before switching to the other plane, and any retuning was done to also transmit 100 % of the beam to the final cup. The deflector was also rotated to check the other plane, and the quadrupoles retuned to provide 100 %. In general, this procedure did not provide 100 % transmission when deflecting a test beam up to 40 mrad in the four cardinal directions. This procedure was used for the single full angular acceptance measurement.

Additionally, since the angular and energy acceptance is dependent on the beam extent and shape at focal plane F_2 , the WF quartz was used to aide in tuning Q_{1-7} to their proper values. The beam should move minimally at this location when deflected up to the maximum 40 mrad in any direction. The beam profile is required to be horizontally narrow for the highest mass separation, requiring the vertical extent to be large. Using this intermediate quartz slightly improved the ability to tune the separator but did not allow for a full angular acceptance measurement to be performed.

Degrader foil: The limiting factor in using the deflector plates as the only angular change is that each direction must be looked at independently. Assuming the plates are aligned to deflect in the horizontal direction, only one direction (left or right from the beam's perspective) can be viewed at a time without some manual adjustment to the deflector plate power supply. The cyclic problem of correcting the beam trajectory only to remove that correction becomes harder to avoid. Since the plates can only deflect along a single plane, the additional unknowns of removing a large angular acceptance along a difference by making changes on the current plane also decreased the possibility of success.

At the target location, Al foils of different thicknesses were placed to degrade the beam, creating a spread in angle and energy at the same time. Foil thicknesses were matched with beam properties to fall within the anticipated $\Delta E/E = \pm 8\%$ and $\Delta\theta = \pm 40$ mrad acceptances of St. George. Since the foils also induce an energy loss for the test beam, the separator dipoles needed to be properly scaled down to the correct values after the test beam (without foil in place) was aligned to the magnetic optical axis. The scaling required accurate and precise measurements of the foil thicknesses. Thicknesses ranged from $100 - 250 \mu\text{g}/\text{cm}^2$, and ^1H and ^4He test beams in the energy range of $0.9 - 2.0$ MeV were used.

Using the WF quartz, the test beam was tuned to have the correct phase space

properties at F_2 . The degraded test beam is emitted into the separator within a phase space determined by its interaction with the foil, allowing the magnets to be tuned without relying on the slow change between deflection angles and directions and including the minor energy acceptance measurement. Currently, no full angular acceptance measurements have been made past F_2 .

Reaction Measurement: Additional measurements have been made of the angular acceptance with an energy acceptance and a nearly achromatic focus at the F_2 focal plane. These measurements were for the altered settings for transporting α particles from (p, α) reactions. The measurements are a different “proof of concept” for the angular acceptance measurements by verifying a $\Delta\theta = \pm 40$ mrad acceptance with the deflector plates before using a foil to produce the full angular spread. In this case (see [SECTION]), the transported particles are the reaction product α particles, verified using a direct test beam of $^4\text{He}^{2+}$. The transported reactions products within the ≈ 45 mrad cone limited by the target Faraday cup were transported to F_2 and detected with the Si detector.

3.4 Considerations

Full acceptance measurements require a fine detailed understanding of the operation of St. George. Previous work has provided the initial understanding on providing a large energy acceptance of at least $\Delta E/E = \pm 8\%$ and angular acceptances near $\Delta\theta = \pm 40$ mrad. Combined measurements have been limited to a large energy acceptance and small angular acceptance or vice versa. Current work is ongoing on providing an improved understanding of the operation of St. George, particularly in setting the quadrupole fields.

A full commissioning of the separator system requires the gas target, separator, and detection system to be operated in parallel and well-understood. The current status of each of these discrete systems is varied. The Hippo gas target has been tested

in a prior configuration, and work has been started to redesign the upper chamber to improve the possibility for monitoring incident beam current and using a γ detector in coincidence with the final detector system. The combined $E_{\text{TOTAL}} vs. TOF$ detection system has been shown to work for test surface sources. Silicon detectors are known to be very robust, and the Si detector and acquisition system has been used for a successful measurement with St. George for (p, α) measurements. The separator status has been explored earlier in this chapter. Final verification of the separator will be measuring the test reaction $^{14}\text{N}(\alpha, \gamma)^{18}\text{F}$ in inverse kinematics.

The target chamber used for the commissioning work and the experimental campaign is different than that which will be used during a fully featured St. George experimental campaign, namely the Hippo supersonic helium gas jet target. Hippo will be used for (α, γ) experiments following the completion of the commissioning work. The specifics of that gas target are discussed elsewhere (see [9] and [11]). Due to the differences between the commissioning chamber and the design of the gas target, some specifics of beam tuning and preparation (see Sec. 3.3.1) will inevitably change as experimental work transitions between commissioning and reaction research work.

CHAPTER 4

MEASURING THE $^{27}\text{Al}(\text{p}, \alpha)^{24}\text{Mg}$ CROSS SECTION

An experimental campaign to study the $^{27}\text{Al}(\text{p}, \alpha)^{24}\text{Mg}$ reaction with the St. George recoil separator was undertaken at the NSL. Runs were completed in December 2016 and February 2017, with runs focusing on determining the correct magnetic fields within St. George completed in Fall 2016 and February 2017. Two low energy resonances were measured with beam currents in the $2 - 3 \mu\text{A}$ range in February 2017. Studying this reaction provides a test of the angular and energy acceptances of St. George in preparation for studying (α, γ) reactions across a wide range of targets and energies.

The first portion of these runs fall under general St. George commissioning work as discussed in Chapter 2 and will not be repeated here. The second portion of the runs involved characterizing the target and the detector, finalizing the optimal settings for the separator, and performing the experiment. The reaction of interest produces α particles in the energy range of $2 - 3 \text{ MeV}$ for the desired proton energy range.

4.1 Altered Tune

The magnet settings for St. George were determined to transport α particles, where the entirety of the particle envelope is described by a characteristic energy and angular [term]. The produced α particles had a low (values?) energy spread and a high angular spread, where only those particles emitted within the desired 40 mrad

acceptance cone for St. George were tuned to reach the detector focal plane F_2 after the Wien filter and impinge the installed Si strip detector.

The restrictions on the beam spot for measuring $(p\alpha)$ reactions at this focal plane require an approximately symmetric spot size in both directions and one that is smaller than the physical face of the detector, whereas the standard tune for studying (α, γ) reactions required that beam spot to be asymmetric with the beam spot being narrow in the dispersive x -plane and tall in the y -plane. The initial COSY code for St. George (see Section 3.1) was altered to model the shortened separator and provide information on the beam characteristics at the new detector focal plane. The magnetic field settings for the seven quadrupoles Q_{1-7} were adjusted to transport the recoil particles to the detector plane with a final beam spot no larger than the face of the Si detector of 58×58 mm. Final pole tip fields are given in Table 4.1.

For the (p, α) experiment, the transported α particles have the properties listed in Table 4.2. The incident proton beam is rejected within the COSY ion optics solution after the first dipole doublet B_1B_2 , and the beam properties are not listed here.

4.2 Experimental Considerations

4.2.1 Beam Reduction

Incident proton beam reduction on the order of $10^{10} - 10^{14}$ are required to avoid damaging the Si detector and observing off-resonance yields of the produced α particles. These limits are within the designed capabilities of St. George but must be verified experimentally

TABLE 4.1

POLE TIP FIELDS FOR (α, γ) AND (p, α) STUDIES

Quadrupole	Pole Tip Field [T]	
	(α, γ)	(p, α)
1	-0.163 032 76	-0.157
2	0.188 823 63	0.187
3	0.093 841 48	0.094 11
4	-0.126 204 02	-0.04
5	0.100 324 05	0.092
6	0.046 936 54	0.0585
7	0.0	-0.015
8	-0.097 791 79	
9	0.174 396 27	
10	0.210 922 28	
11	-0.139 623 55	

TABLE 4.2

ALPHA PARTICLE PROPERTIES

Property [Unit]	Value
Energy [MeV]	2.504
Δ Energy [%]	3
Angular spread [mrad]	40
Target diameter [mm]	3
Q [e]	2
$B\rho$ [Tm]	0.228
$E\rho$ [MV]	4.0

4.3 Procedure

The procedure for performing the $^{27}\text{Al}(\text{p},\alpha)^{24}\text{Mg}$ measurements is divided between the experimental procedure and the procedure to measure a single energy point for clarity. Verification of the initial field settings of St. George was discussed in Section [REFERENCE] as is assumed for the remainder of this discussion.

4.3.1 Campaign Procedure

4.3.2 Run Procedure

At each energy point, preliminary runs were performed to verify the field settings of St. George and determine the systematic uncertainties of the tune. Following these checks, a final measurement at that energy was performed until the statistical uncertainty was below 1 % for on-resonance points and below 5 % for off-resonance points.

4.4 Data Reduction and Analysis

Each region of interest covered a single narrow resonance from the $^{27}\text{Al}(\text{p}, \alpha)^{24}\text{Mg}$ reaction. Extraction of resonance parameters from these regions required a data analysis pipeline to process the individual spectra from each strip of the Si detector and the detector spectra as a whole. Detection systematic uncertainties were determined individually for each energy measure prior to the final measurement at that energy. Target effects on the incident beam and produced α particles were explored [HOW?].

4.4.1 Experimental Systematics

The properties of the target, detector, and separator for the given experiment were explored through various means before, during, and after the data collection phase. Where applicable, the properties were compared to anticipated or predicted values. Differences between operating and testing conditions may be a cause of certain discrepancies within the detector spectra, as discussed below.

4.4.1.1 Target Properties

The self-supporting ^{27}Al target was measured to have a thickness of $62.50 \pm 0.05 \mu\text{g}/\text{cm}^2$. Target thickness was measured using an offline detector station with a $^{241}\text{Am}/^{148}\text{Gd}$ mixed α source. Runs with and without the target foil between the source and the detector lasted 600 s. The annular Si detector was not able to resolve the lowest intensity ^{241}Am peak during the runs, and only the highest intensity peak could be reliably resolved in the spectrum obtained with the target in place. The two spectra are shown in Fig. 4.1, and the α -particle peaks are given in Table 4.3.

The spectra were calibrated from the source-only run using the known energies of the emitted peaks. The shift in energy of the two largest peaks were recorded. The expected range for each peak was determined by interpolating the tabulated

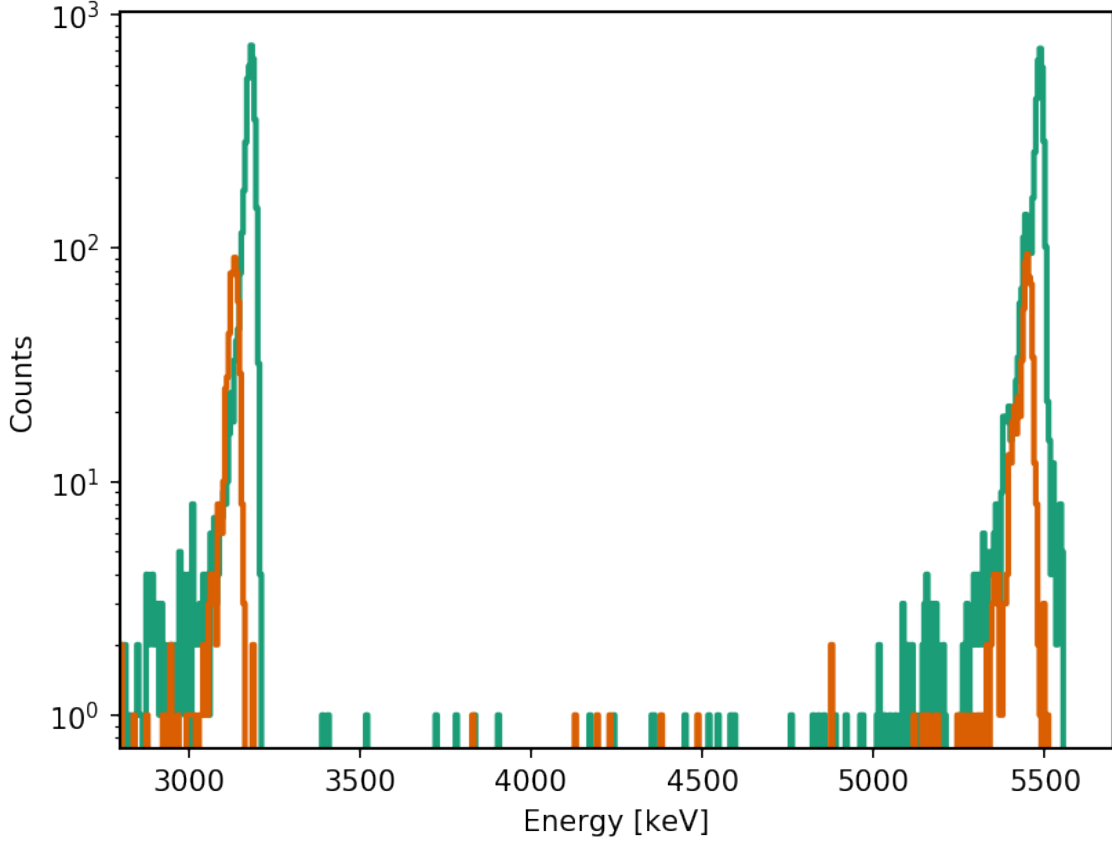


Figure 4.1. Target thickness measurement, showing the shift in the α peaks to lower energies due to the presence of the target. The initial spectrum is in green and the degraded spectrum is in orange. Only the energy range of interest is shown.

results from SRIM [15]. The target thickness was the difference in range for each peak between the degraded and undegraded α energies.

During the experiment, the total time of beam on target was minimized to limit the amount of carbon deposited on the target. Total charge accumulation on the order of 100 mC, with ≈ 75 mC from the final measurement runs. The longest measurement run deposited ≈ 25 mC on the target. At these levels, no appreciable change to the target thickness during the experiment could be seen. The target thickness was not remeasured following the end of the experimental campaign.

TABLE 4.3

ALPHA PARTICLE ENERGIES FOR $^{241}\text{Am}/^{148}\text{Gd}$ MIXED SOURCE

Isotope	E_α [keV]	Intensity
^{148}Gd	3182.69	100 %
^{241}Am	5388	1.6 %
	5442.8	13.1 %
	5485.56	84.8 %

4.4.1.2 Detector Properties

The 16-strip Si detector was calibrated using a $^{241}\text{Am}/^{148}\text{Gd}$ mixed α source. Calibration runs were taken before and after the data collection phase, since the bias voltage was changed for the final runs. The final calibration run was taken with the same electronics setup and detector installation as during the run, except that the beam shield was removed.

Each strip and ADC were calibrated separately. A linear fit was used, as there only the two highest intensity α -particle peaks were resolved. Bins were shown to be approximately 2 keV for every strip. The resolution is cited for only the $E_\alpha = 3182.69$ keV peak from ^{148}Gd as this is closer in energy to our expected particles. The calibration constants and detector resolutions are shown in Table 4.4.

The efficiencies of the individual strips were not determined and assumed to be 100 % for all. Measurements of similar detectors for the St. George detector system commissioning work showed $> 99\%$ efficiencies across all strips.

The detector response shows low energy tails for both alpha peaks (see Fig. 4.2). The data show that the α events may fall outside of the two peaks. All events within our detector can then be considered real events, reducing the reliance on the energy

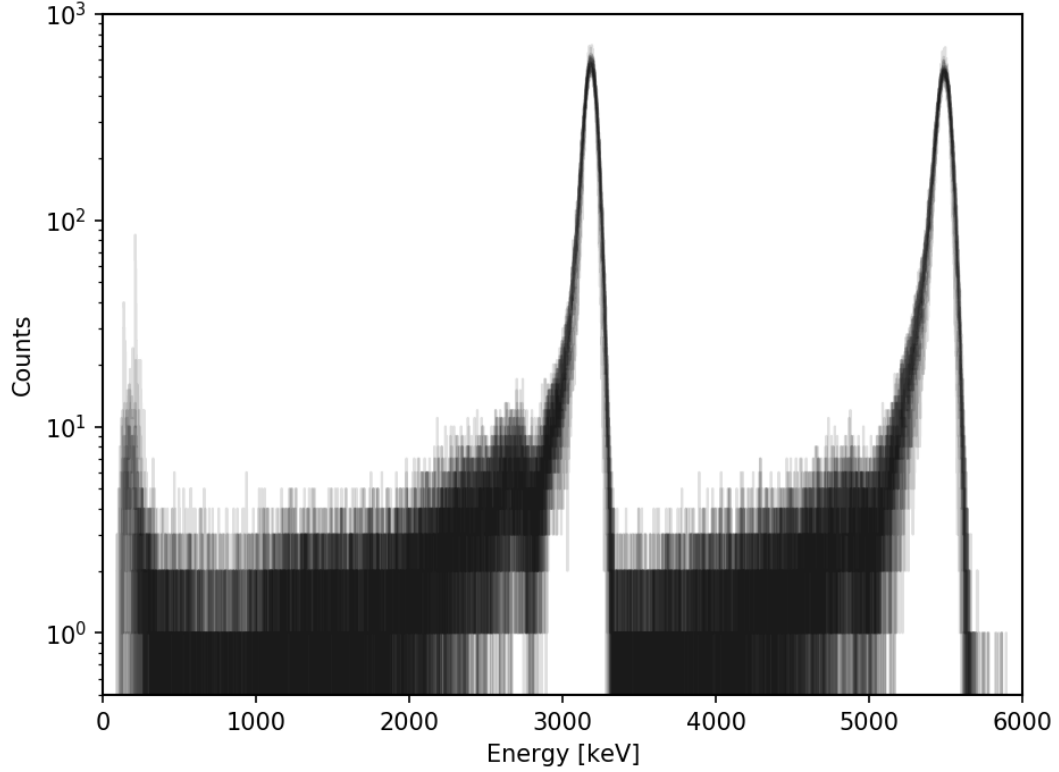


Figure 4.2. Example of the detector response from the energy calibration run. All 16 calibrated strips are overlaid to better show the overall trend. Long, low-energy tails from both calibration peaks can be seen. The counts in the lowest energy range are noise.

calibration. The data also shows that the lower intensity ^{241}Am α peaks cannot be resolved.

4.4.1.3 Separator Properties

The energy resolving power is the minimum energy difference required to resolve a peak from the central image peak assuming that the change in energy is the only difference between the two peaks. By definition this quantity is only a first-order value, so only those parameters with a linear relationship with the position need be

TABLE 4.4

DETECTOR ENERGY CALIBRATION AND RESOLUTION

Strip	a_0 [keV]	a_1 [keV/ch]	Resolution
1	-85.61	1.6534	1.92 %
2	-165.12	1.7327	2.67 %
3	-123.66	1.5791	2.38 %
4	-172.41	1.6824	2.71 %
5	-194.53	1.6923	2.71 %
6	-235.36	1.7636	2.88 %
7	-202.59	1.7946	2.99 %
8	-203.93	1.8526	2.85 %
9	-269.19	1.8725	3.00 %
10	-252.46	1.8166	3.03 %
11	-243.02	1.8509	2.91 %
12	-272.25	1.8291	2.87 %
13	-235.06	1.8161	2.97 %
14	-172.81	1.7601	2.77 %
15	-235.26	1.8246	3.10 %
16	-110.00	1.6412	2.17 %

considered. The energy resolving power of the separator in relation to the terms present in the COSY transport map is defined as

$$\delta_k(\text{RP}) \equiv \frac{2[(x|x)x_0 + (x|a)a_0]}{(x|\delta_k)}, \quad (4.1)$$

where x_0 and a_0 are the initial half-widths for position (in meters) and angle (in radians), respectively, and the remaining terms are the values from the transport map. The resolving power is only taken in the horizontal plane due to the vertical symmetry of the separator. The terms taken from the transport map are

$$(x|x) = 2.261610$$

$$(x|a) = -0.1368242$$

$$(x|\delta_k) = -0.2774295,$$

where signs are conserved for completeness. The maximal deviation caused by each terms is taken to be a positive value. The half-widths x_0 and a_0 are physically limited by the target chamber and taken to be $x_0 = 1.5$ mm and $a_0 = 42$ mrad, giving a resolving power of $\delta_k(\text{RP}) = 0.286$. Since the produced α particles have an inherent spread in energy due to the incoming beam and the particles themselves interacting with the target, the energy resolution should be viewed as the window within which the energies are indistinguishable. As this window covers the expected energy spread of the produced α particles, there are no energy corrections required across the detector strips.

4.4.2 Yield Extraction

For each energy, the number of α -particle ejectiles produced was the total sum of counts within each detector strip above the maximum proton energy. Due to the

detector response, any event above the noise threshold at ≈ 200 keV is a potential α event. There is still the possibility that some of the incident proton beam strikes the detector despite the rejection capabilities of St. George, so those counts below the maximum proton energy are rejected. The maximum proton energy is taken as the incident beam energy plus 3 % to be conservative. Since the proton beam is degraded in energy based on its interaction with the thin foil, this upper limit for the proton energy and lower limit for the α energy range will prevent any proton-induced counts from being counted. An example is shown in Fig. 4.3. While most runs did not show a discernible peak at the expected energy, this cut was still made. In those cases, “lost” counts were smaller than the statistical uncertainty of the counts above the energy threshold.

Beam currents at the target location were recorded before and after each run. For runs lasting longer than 15 m, the current was recorded every 15 m. The beam current was seen to fluctuate around the recorded value by up to 100 nA. For runs with multiple current readings, the average was taken as the nominal current. Time on target was recorded by the acquisition system.

The total yield for each energy is given by $Y(E) = N_r/N_b$, where N_r is the number of reaction products produced and N_b is the number of incident beam particles. If we include the detector and transport efficiency of our setup, and relate N_b to our incident beam current, our yield becomes

$$Y(E) = \frac{N_r}{\epsilon_d \epsilon_t I_b t}. \quad (4.2)$$

In this case, we assume that the detector and transport efficiencies are 100 %, based on the usage of a Si detector and the setting of St. George to create a 100 % transmission state.

The uncertainties in the number of incident beam particles come from the un-

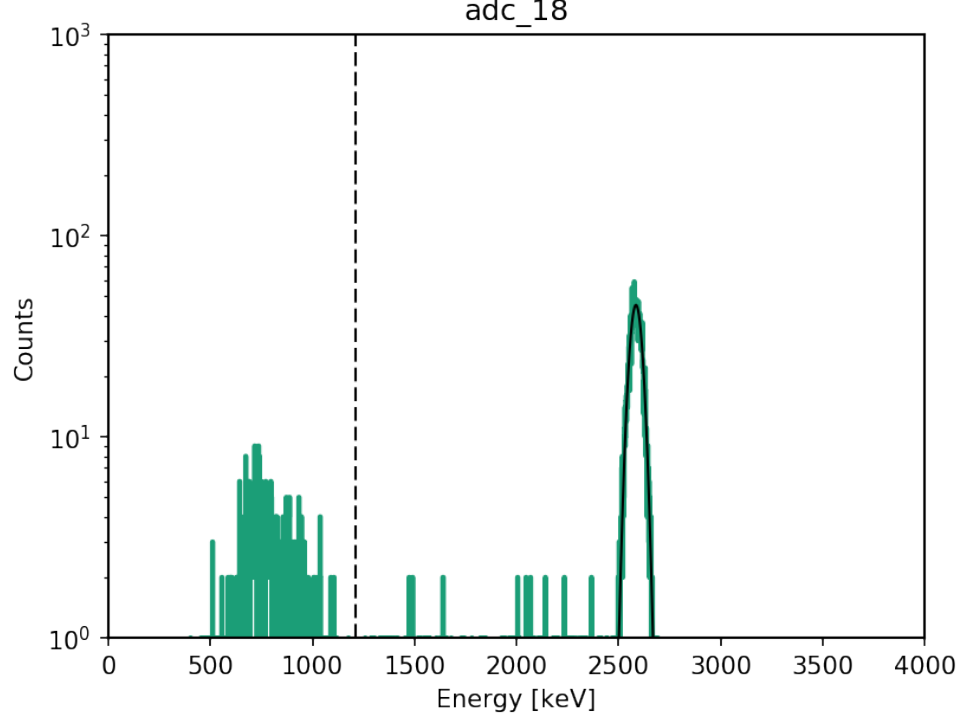


Figure 4.3. Possible proton peak within the spectrum of a single ADC. Data is from Run 241 ($E_p = 1.1781$ MeV). The vertical dashed line shows the energy cut, with the potential beam peak below this energy. The remaining 15 strips for this run showed a similar peak in both central energy and counts.

certainty in the collection time at the detector and the uncertainty or walk within the incident beam current arriving at the target location. Due to the start-up and shut-down timing for the DAQ, a time uncertainty of 5 s was adopted for each run, which should be a conservative value. Without the offset Si detector to measure scattering at the target, we do not have a direct measure of the beam current *in situ* and must rely on the beam currents measured before and after a given experimental run. From those measurements, and from previous experimental runs using the 5U, an uncertainty of $0.1 \mu\text{A}$ (less than 5% in most cases) was adopted. Final uncertainty for the number of incident particles is thus below a 5% statistical threshold.

The uncertainty in the number of reaction products produced can be divided

between the statistical uncertainty in the counting of particles at the detector and the systematic uncertainty of the missed particles at the detector plane due to the tuning of the magnetic and electrostatic elements of St. George. The statistical uncertainty of the counts is $\approx 5\%$, as experimental runs were continued until this point. The systematic uncertainty can be approximated by using the additional runs performed before the actual experimental run, used to finalize the tune of the Wien filter and to estimate the loss below the detector position, to estimate the “lost” counts arising from the final experimental configuration of the separator.

The mounted target is a $62.50 \pm 0.05 \mu\text{g}/\text{cm}^2$ self-supporting Al foil provided by Dr. Simon’s group at the NSL. The target thickness was determined with a mixed $^{241}\text{Am}/^{148}\text{Gd}$ α source, providing α particles across the expected energy range, as shown in Table [REFERENCE]. Only the two highest intensity peaks in ^{241}Am could be reliably discriminated from the background, thus providing only three energy points for calibration purposes of the detector. Target thicknesses were measured using an offline setup, consisting of a Si detector within a vacuum chamber connected to a data acquisition system. Data was recorded using MAESTRO for Windows [REFERENCE] and converted using `pyne`.

4.5 Detector Spectrum Verification

Due to the suboptimal energy resolution of the Si strip detector, caused by the decreased bias voltage and increased leakage current, a well-defined spectrum for the produced α particles was not obtained. The spectra for each run and each strip show a wide peak at the expected location of the α energy peak which we need to verify that it represents the same underlying expected energy peak produced in the reaction. This final verification is a convolution of the incident beam energy, the properties of the target, the cross section domain that we are probing, and the energy resolution of the detector. Each of these components will be discussed in turn.

To reduce this check to a smaller subset of possibilities, only the two resonance energy runs will be checked, but the same process described below can be repeated for any energy in question, given the existence of the required files to support the analysis.

This analysis relies on the usage of SRIM/TRIM [CITE] to generate the files describing the target effects, and those files should be generated according to the steps described below before the analysis is begun. The file generation can be done programmatically following the SRIM user guide, or “by hand” using the included GUI, both of which are standard procedures and will not be discussed here.

4.5.1 Assumptions

In order to fully describe reaction process from incident beam to detector energy spectrum, we must make some assumptions and check that they are approximately true for the desired reaction.

First, the stopping power of the target must be slowly varying across the width of the target. This assumption reduces the number of required SRIM files, as described below. The definition of “slowly varying” in this case is that the stopping power can be locally modeled as a linear function of the beam energy, and that the coefficient relating the energy to the stopping power be relatively small.

Second, knowledge of the underlying cross section is required. The procedure described below can be inverted slightly to move from the detector energy spectrum to the reaction cross section, knowing all other parts, but this more-complex procedure was not required for the reaction in question. Using known resonance properties, the $^{27}\text{Al}(rmp, \alpha)$ reaction cross section can be modeled with the AZURE [CITE] *R*-Matrix code to produce the file. The energies returned from this code should be transformed into lab coordinates.

Third, the target should be thin enough that the beam can pass through the target

relatively unimpeded. Should this assumption not be met, the procedure outlined must be updated to account for the additional straggling, especially where the exit angle of the particles is sufficiently spread out.

Finally, the thickness of the target in energy for the incident beam energies must be known. Given that the thickness in mg/cm^2 can be measured using standard techniques, the thickness in energy can be determined by

$$EQUATIONHERE,$$

where dE/dx is the stopping power in units of [UNITS]. The target thickness only needs to be determined for the incident beam, as this defines the cross section energy domain.

The additional knowledge required to perform the following analysis, such as the incident beam energy uncertainty and the detector energy resolution, will not be discussed separately.

4.5.2 Required SRIM Files

The pre-generation of SRIM files requires special note to justify the energy and depths used. In cases where the incident beam energy spread is greater, the target is thicker, the stopping power varies quickly, or any other deviation from the assumptions above, the procedure below must be amended and additional SRIM files will most likely need to be generated to account for those changes.

The incident beam files describe the target effects on the beam energy at multiple depths within the target. To simplify, all incident particles are assumed to strike the target perpendicular to the target, and the angles for each particle following their interaction with the target are saved but not used within the analysis. While the primary goal of this portion of the analysis is verifying the energy spectrum, the slight

corrections to the energy loss attributed to the angle of the particles, these corrections would be minimal and do not affect the final result. The initial energies chosen for the incident beam protons are the central resonance energies, and the energies chosen for the α particles cover the expected range on possible energies based on previous kinematics studies.

The depths probed for the target are in percents of the total thickness in Angstroms. For this analysis, depths from 1 to 99 % in steps of 2 % were used, which provides adequate coverage of the energy loss through the target while minimizing the amount of runs required for SRIM. Both the incident beam protons and the produced α particles require thicknesses across the entire range of the target thickness. Note that depths of 0 and 100 % were not used; depths of zero percent have no meaning for the incident beam case, and depths of 100 % are unphysical since the incident particle will have left the target without reacting.

All files simulated 10k particles, and the final energies of those particles were saved.

4.5.3 Simulating the reaction

The process below describes how the full reaction, from the incident beam to the final detector energy spectrum, can be simulated. The SRIM files required are assumed to be generated beforehand. The process has been wrapped within the `pyne` package under the `tree` submodule, which takes as input the path to the generated files and the masses and energies of the particles in question.

4.5.3.1 Simulating the incident beam

The incident beam energy for the resonance scans were determined by the 5U's analyzing magnet settings. The 5U provides a small energy uncertainty particle beam to the target area, meaning that we have approximately a monoenergetic beam

striking our target. The generated SRIM files for the incident beam are this central beam energy at multiple depths within the target. To simulate the known spread of the beam energy around this central value, the deviation from this central value was randomly assigned, assuming a Gaussian distribution of energies. The individual particle energies are given as

$$E_i \sim E_{\text{Resonance}} + \text{Normal}(0, \sigma),$$

where $\sigma = 300$ eV is the measured beam energy uncertainty of the 5U.

The cross section that the incident particles will probe is defined by the initial energy of the beam and the thickness of the target in units of energy. For the target in question, the energy thickness is approximately 10 keV for both resonances. The cross section within this energy domain was determined for the central resonance energy, which is an approximation that initially ignores the energy spread of the beam. As this energy spread is less than 0.1 %, the effect of this choice is minimal and helps to simplify the process since a single probability distribution for the cross section needs to be determined. The cross section within the energy range is divided into energy bins of 1 %, with the values interpolated where the results of the R -matrix calculation do not match with the integer depth values. These depths are then randomly chosen based on the normalized cross section in that region. An example is shown in [FIGURE].

[FIGURE]

Once a simulated depth is assigned to each particle, the SRIM results at that depth are used to simulate the final energy of that particle before it reacts with the target. As the energy distributions returned by SRIM are not analytic, we can draw from the 10k simulated values, assuming equal probability for each, which for large sample sizes is approximately equivalent. Each incident particle is now associated

with an initial energy deviation from the resonance energy, the depth at which it reacts, and a final energy at that depth. The initial simulated energy is added to the final energy to give the textitreaction energy of the incident proton.

4.5.3.2 Simulating the produced particles

From these reaction energies, the α energy is determined through basic kinematics. Again, any potential angular spreads are not considered for this stage. As the detected α particles left the target within a solid angle cone of opening angle 40 mrad, we know that we are limited to a small solid angle region that we are actually seeing at the detector. The produced α particles now have an initial energy and a depth within the target, meaning that each particle also has a known target thickness that they must pass through.

The generated α particle SRIM files are used to find the exit energy of the particles in the same way that the final proton energy was found above. In this case, instead of the energies being defined in reference to a well-defined input energy, the deviation from the closest generated α energy in the SRIM files is used, and that file is used to simulate the exit energy for that particle's depth. The energy deviation is added back to the simulated energy drawn from the samples obtained through SRIM to give a final *exit energy* for that α particle.

4.5.3.3 Detector spectrum comparison

The generated exit energy spectrum of the α particles describes the energy of the recoils as they enter St. George. The angle of these particles can be described by the kinematics of the reaction instead of through the SRIM calculations, so the angle is again ignored for these particles. Since this analysis is focused on the energy spectrum seen at the detector, the angular effects do not need to enter into this calculation.

The energy resolution of the detector was previously measured to be [VALUE] (see [SECTION]), which we must convolve with the exit energy of the α particles. For each particle, a random energy was generated from a Gaussian distribution centered around that particle's exit energy, according to

$$E_{\text{detector}} = \text{Normal}(E_{\text{exit}}, \sigma_{\text{detector}}),$$

where σ_{detector} is the energy resolution of the detector. This final spectrum is a representation of what the experimenter would see from the detector system and must be related to the actual experimental data.

Note that this spectrum assumed that every particle that entered our target reacted, so we can't directly use it to measure the yield. Relating this simulation to the actual spectrum can be done by scaling each particle to the cross section at the location it "reacted", and scaling the number of particles at each final energy by a factor proportional to the determined incident beam current during this experiment. An alternative approach is to scale both the simulated spectrum and the measured spectrum to unit area, which would conserve the number of particles reaching the detector. The previous two options are useful for checking if the calculated reaction rate in the two cases are consistent with each other. A final option would be to see if the two spectra could have been generated from the same underlying distribution, which avoids having to scale either distribution, through a KS test.

The simulated distribution is approximately Gaussian, but the actual distribution is a skewed Gaussian due to the detector response (seen in energy resolution studies too). Not sure how to model this...

4.5.4 SRIM Results

Insert this here, maybe...?

CHAPTER 5

ANALYSIS

The angular acceptance of St. George can be determined by comparing the expected yield from the reaction at the desired energies to the actual counts measured at the detector plane. If we assume a symmetric angular acceptance, the opening angle of the acceptance cone can be directly calculated and compared to the anticipated angular acceptance opening angle of 40 mrad. The angular acceptance and its uncertainty for each energy can be determined independently of the other points. The angular acceptance is based on the properties of the target, incident beam, detector, and recoil separator and the decisions relating to the experiment itself.

All code was written using the scientific Python stack (numpy, scipy, matplotlib, pandas, pymc3). An analysis framework pyne was developed concurrently in python to aide in direct analysis of the run information from the raw data files.

5.1 Target Properties

A self-supporting ^{27}Al target was used for the entirety of the experiment. The target thickness was measured using an offline detector station and a mixed $^{241}\text{Am}/^{148}\text{Gd}$ alpha-particle source. The target thickness was measured by observing the energy loss of the two alpha peaks as compared to the direct detection of the alpha particles by the detector. That energy loss is converted to a target thickness in $\mu\text{g}/\text{cm}^2$ which can be used to determine the energy loss for other particles at any energy. The measured thickness was $63.8^{+2.0}_{-1.7} \mu\text{g}/\text{cm}^2$.

Two runs were performed, one without the target in place and one with the target in place, using an annular Si detector placed within a vacuum chamber. Each run lasted approximately 600 s and were performed immediately following each other. The detector was calibrated using the spectrum from the first run without the target in place, using the known energies of the peaks (see Table XX). The energy calibration parameters were determined through a combined Monte Carlo and Bayesian procedure:

1. New spectra were simulated by sampling a single value for each bin from the Poisson distribution $n \sim \text{Poisson}(\lambda)$, where n is the simulated counts in that bin and λ is the scale parameter for the distribution, which is taken to be the detected counts for that bin. A total of 2000 spectra were generated in this fashion.
2. The two largest peaks were identified first through a continuous wavelet transformation to get an approximate peak center. The final peak center was determined by taking a weighted average of the eleven bins centered on the selected bin to get the final bin value for the peak center.
3. A linear regression is fit, using the peaks found from the simulations and the known calibration energies of the alpha peaks. By fitting the entire sample of peak locations, we determine a global fit for our detector. The linear model used is a Bayesian model described by:

$$E \sim (\mu, \sigma) \mu = \alpha + \beta \text{bin} \quad \alpha \sim (28, 10) \quad \beta \sim (5, 5) \quad \sigma \sim (2, 10)$$

The Bayesian model allows for the uncertainty on the fit to be propagated forward.

Table XX: Alpha-particle energies for the 241Am/148Gd mixed source:

148Gd	3182.69	100
241Am	5388	1.6
	5442.8	13.1
	5485.56	84.8

From the linear model, an energy calibration can be applied to the in-target run to determine the energy of the two largest peaks. Due to the lower count rate due to

the target being in place, only the largest peaks could be identified. The procedure to determine the energy loss is similar to that previously described for the energy calibration:

1. New spectra based on the spectrum with the target in place were generated in the same manner as before. A total of 2000 spectra were generated.
2. For each spectra, a linear model was sampled from the fitted Bayesian linear model and applied to the spectra to convert the bin numbers to energy.
3. The two largest peaks were identified first with a continuous wavelet transformation then a weighted average of the counts to find the central energy of the peak.
4. The energy of the peaks were subtracted from the known energies of the peaks to determine the energy loss through the sample for two known input energies. The uncertainty in the sample alpha energies was assumed to be negligible and was not considered in the calculations.

This energy loss may be related to the target thickness through the use of the computer code SRIM. The stopping and range table for alpha particles passing through ^{27}Al was generated. A linear spline (i.e. each data point from the range table connected by a linear fit) was generated for the range, and the range for each fitted peak energy from the spectra generated from the in-target run was determined. This range was subtracted from the alpha ranges for the known calibration energies and multiplied by the density of aluminium to get the thickness in $\mu\text{g}/\text{cm}^2$. The uncertainties in the calibration alpha energies and in the SRIM data were assumed to be negligible and were not considered during the analysis.

Finally, as each simulated spectra was assumed to be an independent sample, the two thicknesses determined from the two alpha peaks were averaged to get a single value for the thickness from each iteration. The thickness distribution generated in this case was compared against the distribution of 4000 samples (2 dependent thickness measurements for each of the 2000 samples), with the averaged thickness case exhibiting a slightly narrower distribution. The averaged thickness samples

were used for the remainder of the analysis. The thickness of $63.8^{+2.0}_{-1.7} \mu\text{g}/\text{cm}^2$ is the mean and 95 % confidence interval from this distribution of thickness samples. For subsequent calculations, the thickness used was sampled from this distribution.

The uncertainties present in each step of the procedure laid out above are automatically propagated forward due to the methods chosen. The stochastic nature of the process allows the influence of the base assumptions of the underlying data (e.g. the counts in each bin are drawn from a Poisson distribution) to be seamlessly brought forward without the need of cumbersome mathematics that can potentially hide wrong assumptions about the values in question, such as that all of the data is normally distributed.

For most of the following calculations, the number of target nuclei per square centimeter is used instead of the thickness in $\mu\text{g}/\text{cm}^2$. Our target thickness is then $1.42^{+0.06}_{-0.06} \times 10^{18} \text{ nuclei}/\text{cm}^2$. This value is useful for calculating the energy loss of the proton through the target, as that relies on the number density of the target and the stopping power of the material. The energy loss of the beam will be discussed in the next section.

5.2 Beam Properties

The incident proton beam was produced by the 5U and delivered to the St. George target area. The beam energy and resolution were determined through a series of accelerator and beamline commissioning experiments performed before this experiment was performed.

The beam energy was determined from the calibration of the 5U analyzing magnet performed during a different experiment. During the experiment, the magnetic changes were performed slowly such that the magnetic field did not appreciably drift during the runs. The energy resolution can also be determined from the calibration runs, where the resolution is given by the energy width of the leading edge of the

resonance scan. Values of approximately 300 eV were commonly observed, with a conservative value of 500 eV adopted for this experiment since no direct energy calibration was performed with our specific experimental setup. The uncertainty in the analyzing magnet field is accounted for within this uncertainty and is not considered separately.

The beam current was relatively stable during the experiment. During the longer runs, the beam current was measured every 15 minutes in order to monitor its change during the run. For each run, the current uncertainty was determined by the measured values for cases where multiple current measurements were performed, or 5 %. For all runs, the final current uncertainty was between 5 and 12 %. Ideally, an offset Si detector at the target location would be used to monitor the beam current during the entirety of the run by measuring the current of the scattered beam particles at a fixed angle. As this setup was not available for the target chamber, periodic direct measurements of the current using the Faraday cup at the target location were required to measure the beam intensity.

5.3 Detector Properties

A 16-strip Si detector was used to detect the produced alpha particles during the experiment. A calibration run was performed following the experiment using the same detector and data acquisition settings as used during the experiment. A $^{241}\text{Am}/^{148}\text{Gd}$ mixed alpha source was used for calibrating the energy conversion and energy resolution of each strip separately. All of the strips were similar with approximately 2 keV/bin for the calibration and approximately 2.75 % (90 keV) for the energy resolution.

The calibration run resulted in a single spectrum. Due to the poor energy resolution of the detector resulting from the lower-than-optimal bias voltage setting used during the experiment, only the two highest intensity peaks could be resolved

above the background. As the alpha peak resulting from ^{148}Gd is closer in energy to the alpha particles produced in the experiment, The alpha peaks also exhibit long low-energy tails such that the particles produced in the reaction are smeared out in energy. For the experimental run, an energy threshold was set to exclude incident proton counts, where counts appearing above the threshold are considered to be from alpha particles. That threshold was set by the following:

$$E_{\text{proton}} + 3\sigma_{\text{beam}} + 3\sigma_{\text{resolution}} \quad (5.1)$$

The detector efficiency was not directly measured and assumed to be 100 %. Efficiency measurements performed during the commissioning work supporting the St. George detector system resulted in efficiencies above 99 % for all strips.

A simulation of the expected energy spectrum at the target location was performed using SRIM data tables. The simulation looked at the known energy loss within the target of the incident beam, the expected cross section within the energy limits of the target, the energy loss of the produced alpha particles through the remainder of the target, and the energy resolution of the detector to generate an expected energy spectrum. The procedure for this simulation is as follows:

1. An energy deviation drawn from the Normal(0, sigma) distribution (where sigma is the beam energy resolution) for 2000 particles. This energy deviation is the difference in energy from the central energy.
2. SRIM files for the central energy were generated for fractional depths within the target, where the output is the beam energy profile at that target depth.
3. Using the expected cross section from the AZURE2 R-matrix calculation, a depth for each of the simulated particles was generated to determine the location within the target that the reaction takes place.
4. A beam energy E_d is generated from the distribution of beam energies at the given depth, and the initial deviation for that particle is added to the energy to give the final beam energy.
5. The beam energy is converted to the produced alpha particle energy through the kinematic equation

$$E_{\alpha} = Q + E_p \left(1 - \frac{m_p}{m_p + m} \right)$$

²⁷Al (5.2)

6. The deviation of the alpha particle from a known alpha energy (used to generate SRIM files at various depths) was recorded.
7. An alpha energy was generated for each particle based on the remainder of the target that it needs to travel through from the final energy distribution generated for particles traveling through that thickness.
8. The energy deviation is added back to the alpha particle's energy to give its final energy.

This procedure generates an alpha-particle energy spectrum following the target location given the known parameters about the target thickness and the cross section, and incorporates the known energy resolution of the incident alpha beam and the stochastic nature of the energy loss and reaction within the target. Finally, using the known energy resolution of the detector, a final energy spectrum can be generated by drawing new alpha particle energies from the distribution:

$$E_{\alpha, \text{detector}} \sim (E_{\alpha}, \sigma_{\text{detector}}) \quad (5.3)$$

An example of the output of this procedure is given in [FIGURE], where the agreement between the location and width of the alpha peak can be seen in the normalized spectra. Note that the low energy tailing of the detected particles is not modeled in our simulated spectrum, as we don't know the full characteristics for the detector response.

5.4 Additional Parameters

Additional inputs into the final calculation of the acceptance of St. George are the cross section determined from an R-matrix fit on several low-lying resonances,

the stopping power of protons in aluminium from SRIM, the run time, and the counts at the detector. For those parameters that are derived from external programs (AZURE2 and SRIM), the uncertainty is assumed to be negligible. The uncertainty in the time was assumed to be 10 seconds for those runs that only lasted for a single 15-minute span, and higher for those runs that required the periodic measurement of the beam current which resulted in stopping the incident beam for an unspecified duration of time.

The counts at each detector were the sum of all events above the threshold defined by the beam energy and detector resolution. The counts are Poisson distributed, with the length of time for the run was such that the uncertainty from the counts at the detector was not above 5%, with most runs having a count uncertainty of a much lower value. The direct uncertainty of the counts at the detector is partially convolved with the run time; a lower counting uncertainty requires a longer run time and potentially a larger time uncertainty.

The direct beam reduction by St. George must be on the order of $10^{10} - 10^{14}$ in order to avoid damaging the Si detector and to measure lower value regions of the cross section. This requirement is within the designed capabilities of St. George when tuned for heavy recoil transmission to the final detector plane, but must be verified experimentally due to the altered tune and different detector plane required for this experiment. During the experiment, count rates at the detector were monitored, and potential counts from the direct proton beam were excluded from the final counts with the energy discriminator previously described.

5.5 Final Acceptance Measurements

The acceptance of St. George can be found for each energy value by comparing the detected counts to the expected yield for that incident beam energy. The yield is found from:

$$Y(E) = N_r/N_b, \quad (5.4)$$

where N_r is the number of reaction products produced and N_b is the number of incident beam particles. We can determine N_b from the beam current and the total run time. The value for N_r is determined by the total counts at the detector (for the experimental yield) or the integration of target and cross section properties following

$$Y(E_0) = \int \sigma(E)/\epsilon(E) dE \quad (5.5)$$

In both cases, the detector efficiency and St. George transport efficiency are 100 %, as previously discussed.

The acceptance in mrad is given by

$$\theta = \arccos \left(1 - 2 \frac{Y_{\text{experiment}}}{Y_{\text{theory}}} \right) \quad (5.6)$$

The angular acceptance can be calculated in this way for each run individually, as shown in FIGURE and TABLE. The process for calculating the uncertainty bounds is given by the following, repeated 2000 times to have enough confidence in the final values:

1. The beam energy, beam current, and time are sampled from a normal distribution $Normal(\mu, \sigma)$, where μ and σ are for the value (energy, current, or time) in question.
2. The incident number of particles is calculated from the current and time.
3. The target thickness in energy is calculated from finding the stopping power at the incident beam energy from the SRIM tables, and sampling from the distribution of target thicknesses in terms of atoms/cm².
4. The yield is determined by integrating EQUATION between the entrance energy and the lower energy given by that entrance energy minus the target thickness.
5. The experimental yield is drawn from a poisson distribution $Poisson(c)$, where c is the number of counts detected.

6. The acceptance for the iteration is calculated by EQUATION.

The distribution of values generated by the process above can be used to find the acceptance and confidence intervals for the run in question. Each run has an acceptance described by its distribution, which is the run for that particular setting of St. George.

CHAPTER 6

Discussion and Conclusion

The experiment was designed to experimentally confirm an aspect of the acceptance for St. George, specifically the angular acceptance at small energy deviations, using a well-known reaction. Additionally, the experiment aimed to allow for an additional set of reactions to be studied using the facility. The technical capabilities of the separator system were shown to be adequate even with sub-optimal characteristics in the experimental setup, opening up the possibilities of studying low energy (p, α) reactions in the future. The angular acceptance at the peak of the resonances was shown to be consistent with the desired

6.1 Uncertainties

The final uncertainties on the acceptances at each run energy are skewed distributions. Since basic error propagation relies on the errors being gaussian distributed, the fact that our uncertainties are not partially justifies the Bayesian approach described previously. Part of the reason for the skewed distributions is that the acceptance is bounded by zero and $\pi/2$, and since our distributions sit closer to the zero end instead of near the middle of the range somewhat requires that the distribution be skewed.

The uncertainties on most of the inputs are gaussian distributed, as that represents the statistical nature of the process that creates that input value. For example, the beam current is gaussian distributed because...

DISCUSS

The final uncertainty bands for each of the acceptance measurements can be analyzed by what values affect the range for the uncertainty. We can limit this discussion to inputs that are controllable by the experimenter. The final uncertainty will be made up of the uncertainty from inputs and the uncertainty from those statistical and irreducible processes. The four inputs that the experimenter can control are the energy, time, current, and thickness uncertainties. The energy uncertainty is related to the stability of the accelerator and the calibration of the analyzing magnet, both of which can be measured and regulated to the point where the uncertainty can be minimized. The time uncertainty is based on the total runtime and the interruptions caused by requiring the stoppage of the beam in order to measure the current and can be reduced through synchronization of the DAQ with the start of bombardment, and by minimizing interruptions during the data collection process. The current uncertainty can be minimized by measuring the current continuously during the experiment, as there will then be fewer unknown changes in the beam current and a single value for the beam current does not need to be applied to the entirety of the experimental run. Finally, the thickness uncertainty can be minimized by performing target thickness measurements at multiple energies and with potentially multiple particles, and by running those measurements for longer such that the energy loss by the particles can be more accurately determined.

Each of these inputs affects a different part of the final acceptance, based on how it relates to the experimental and theoretical yield, or both. We can determine the impact of reducing the uncertainty on each of these inputs by setting the uncertainty to zero within the analysis pipeline, which would return a different uncertainty band for the run in question. Since these uncertainties are not necessarily independent of each other, we should also look at all combinations of these four inputs being controlled for to get a full picture of the impartances. Additionally, the irreducible uncertainty can be determined by keeping all of the inputs constant. The contribution

to the final uncertainty is expressed as a percent of the total uncertainty band for both the 67% and 95% confidence interval, so the amount of the band that is accounted for by the inputs that are not held constant.

TABLE₆7TABLE₉5

From these tables, we observe a few interesting trends that we can leverage during follow-up experiments to improve the final uncertainty of the acceptance and from that the uncertainty on the experimental yield. The trends are...

DISCUSS

6.2 Uniformity of Acceptances

When calculating the acceptance for St. George, it was assumed that the acceptance cone was described by a single opening angle. In practice, the horizontal and vertical opening angles may be distinct from each other. During preliminary experiments for the acceptance of St. George, it required much less fine tuning of magnetic fields to achieve the maximum vertical acceptance than it was to achieve the maximum horizontal acceptance. This observation may be due to the lack of dispersive elements in the vertical plane.

The strips of the Si detector were aligned such that an individual strip was oriented in the vertical direction, or a particle that is deflected horizontally would be detected on a different strip (see FIGURE). This orientation allowed for improved tuning in the horizontal plane with the lack of sensitivity in the vertical plane. The auxiliary runs performed where the detector was placed in the “low” position (where the top of the detector is located where the bottom of the detector would be in the regular running position) inform the amount of particles that are not captured in the vertical plane due to minor mistuning of the separator, and the auxiliary runs used to center the produced alpha particle distribution on the detector horizontally inform the amount of particles that are not captured in the horizontal direction. Ideally, a detector

segmented in both the horizontal and vertical plane would give a full description of the alpha-particle beam spot density at the detector plane and could be used to better relate the distribution of counts at the detector plane to the acceptance cone at the target location.

In the final configuration of the target system, a series of conical collimators will be located following the target location to define the 40 mrad acceptance cone. As the desired configuration of St. George is to measure (α, γ) reactions where the heavy recoil particles are emitted from the target within a cone with an opening angle less than 40 mrad, NOTES. For experiments similar to this where the ejected particles are emitted within a cone larger than 40 mrad, these collimators would ensure that the particles reaching the final detector must have been emitted within that known acceptance cone. This restriction would improve the tuning of the separator for similar experiments, as the emitted particle beam spot at the detector plane can be more easily tuned to fit completely on the detector.

6.3 Potential Sources of Error

The preliminary tunes were determined by keeping a beam with a given energy and angular deviation from the mean reached the detector plane within the physical space of the detector as measured on a quartz.

6.4 The (p, α_1) channel

At the resonances probed, the (p, α_1) reaction channel is also open. Measuring the cross section for this reaction at the two desired resonances is a more difficult experiment due to the lower rigidity of the produced alpha particles due to the lower energy. The kinematics for this reaction are given in TABLE.

The lower rigidity is still within the design parameters of St. George, but due to the altered tune required to direct the produced alpha particles to the detector

plane has different rejection properties than the standard tune. As such, the incident proton beam is close enough in rigidity that the beam may strike the detector. The beam reduction levels would not be high enough to avoid damaging the Si detector, preventing the measurement of the cross section without either additional rejection capabilities or an improvement in the tune.

MORE DETAILS FROM LOGBOOK

6.5 Requirements for Replication and Improvement

6.6 Next Steps

6.7 Closing Thoughts

APPENDIX A

POLE TIP FIELDS

For the two possible reaction study settings for St. George, the fields required are different. The difference arises from the difference in required recoil properties at the post-Wien filter focal plane F_2 . The pole tip field settings for (α, γ) experiments are from using a mass $A = 41$ recoil in charge state $Q = 11^+$ with rigidities $B\rho = 0.331$ Tm and $E\rho = 2.836$ MV (see Figure 3.1 for more details).

APPENDIX B

RUN INFORMATION

Additional information about the $^{27}\text{Al}(\text{p}, \alpha)^{24}\text{Mg}$ productions runs.

TABLE B.1

RUN ENERGY DETAILS

Run Numbers	Field [G]	E_p [MeV]	E_α [MeV]
261—264	1693.3	1.363 18	2.7700
265—270 [†]	1690.4	1.358 52	2.7655
271—277	1687.1	1.353 22	2.7604
278—282	1683.9	1.348 09	2.7554
283—288	1680.1	1.342 01	2.7495
242—248	1580.8	1.188 07	2.5996
251—255	1577.5	1.183 11	2.5948
256—260 [†]	1574.6	1.178 76	2.5905
229—234	1571.4	1.173 98	2.5859
235—241	1567.9	1.168 75	2.5808

†: Denotes runs at resonance energy

APPENDIX C

DEFLECTOR SETTINGS

Deflector settings used for commissioning work. Voltages are based on the physical characteristics of the deflector system and the beam properties to provide the necessary deflection. Setpoints are based on the version of the control program in place at the time of the experiments.

TABLE C.1

DEFLECTOR SETTINGS FOR TEST BEAMS

Angle [mrad]	$^1\text{H}^+$ at 1 MeV		$^4\text{He}^+$ at 2.3 MeV	
	Voltage [kV]	Setpoint	Voltage [kV]	Setpoint
5	0.363	9	0.834	24
10	0.725	20	1.668	49
15	1.087	31	2.501	74
20	1.450	42	3.335	100
25	1.813	53	4.170	125
30	2.176	64	5.004	150
35	2.539	75	5.839	175
40	2.902	86	6.674	201
45	3.265	97	7.509	226

APPENDIX D

ANALYSIS PACKAGE

The analysis and plots contained within this dissertation were completed using Python and a small set of standard scientific python packages:

- *NumPy*: a standard numeric package that adds array (vector and matrix) computing;
- *Scipy*: a scientific utilities package built on top of NumPy that includes general-purpose routines such as curve fitting, root finding, signal processing and more; and
- *Matplotlib*: a 2D plotting package that supports multiple backends and output formats.

These three packages are standard components of the Python Scientific Stack, and their usage and internals are well-documented and trusted by many scientists in multiple fields. The usage of Python in the scientific community has increased steadily over the years, with multiple special purpose packages built on top of the foundation of these three packages, particularly NumPy.

For the actual analysis, a two-part analysis framework was developed in tandem with the analysis work: Python for Nuclear Experiments (PyNE) and the St. George Analysis Package (SAP). These packages are designed to be extensible by other research groups, guided by the requirements of the St. George group, while providing an easy-to-use and understand object-oriented interface to performing nuclear astrophysics research. Development work was chronicled on the packages' GitHub page¹, and may be installed from there.

¹<https://github.com/mmoran0032/pyne>

These packages would not be possible without two other important packages: the ROOT² Data Analysis Framework[3] and `evt2root`³. The decision to not use these packages (and thus, C++) for the analysis will be discussed following the description of the packages themselves.

D.1 Python for Nuclear Experiments

D.2 St. George Analysis Package

D.3 Justification

The `pyne` (Python for Nuclear Experiments) data framework is based on two main analysis codes and frameworks: the ROOT data analysis framework, and Dr. Karl Smith’s `evt2root` conversion utility. The `pyne` environment is designed to be similar to these packages, but since its development was alongside the analysis done for this experiment, additional functionality not needed for this analysis was not included. In particular, the buffer file processing only handles `.evt` and `.Chn` files, and the crate focus was on just a single ADC module. Additionally, most of the analysis work with these basic structures should be done using a separate package (such as the `sap` (St. George Analysis Package)), and keeping the two responsibilities of data conversion and structure and analysis of said data results in cleaner code for the user.

Development of `pyne` started in March 2016, and the current version can be found on the package’s GitHub page. Within that same repository is the `sap` package, but that code is not reproduced here. The code listed is from version 0.6.0 (updated on May 12, 2017). The packages outside of the Python standard library required for use are `numpy`, a standard numeric package for scientific Python, `scipy`, a scientific

²<http://root.cern.ch/>

³<https://github.com/ksmith0/evt2root>

analysis package built on top of `numpy`, and `matplotlib`, a 2D plotting interface. All three of these packages are standards for scientific computing with Python. Currently, only Python 3.X is supported. As official support for Python 2.7 is set to terminate in 2020, and most scientific package managers have already switched to Python 3.X, this decision is warranted.

BIBLIOGRAPHY

1. C. Angulo, M. Couder, S. Cherubini, W. Galster, J.-S. Graulich, P. Leleux, F. Vanderbist, and A. Shotter. *Nuclear Physics A*, 688(1):462 – 464, 2001. ISSN 0375-9474. doi: [http://dx.doi.org/10.1016/S0375-9474\(01\)00756-4](http://dx.doi.org/10.1016/S0375-9474(01)00756-4). URL <http://www.sciencedirect.com/science/article/pii/S0375947401007564>. Nuclei in the Cosmos.
2. R. Baartman and D. Kaltchev. *Proceedings of PAC2007*, pages 3229 – 3231, 2007. doi: 10.1109/PAC.2007.4440381.
3. R. Brun and F. Rademakers. Root - an object oriented data analysis framework, September 1996. URL <http://root.cern.ch/>.
4. M. Couder, C. Angulo, W. Galster, J.-S. Graulich, P. Leleux, P. Lipnik, G. Tabacaru, and F. Vanderbist. *Nuclear Instruments and Methods in Physics Research Section A: Accelerators, Spectrometers, Detectors and Associated Equipment*, 506(1):26 – 34, 2003. ISSN 0168-9002. doi: [https://doi.org/10.1016/S0168-9002\(03\)01381-0](https://doi.org/10.1016/S0168-9002(03)01381-0). URL <http://www.sciencedirect.com/science/article/pii/S0168900203013810>.
5. M. Couder, G. P. A. Berg, J. Görres, P. J. LeBlanc, L. O. Lamm, E. Stech, M. Wiescher, and J. Hinnefeld. *Nuclear Instruments and Methods in Physics Research, Section A: Accelerators, Spectrometers, Detectors and Associated Equipment*, 587:35–45, Mar. 2008. doi: 10.1016/j.nima.2007.11.069.
6. S. Engel, D. Hutcheon, S. Bishop, L. Buchmann, J. Caggiano, M. Chatterjee, A. Chen, J. DAuria, D. Gigliotti, U. Greife, et al. *Nuclear Instruments and Methods in Physics Research Section A: Accelerators, Spectrometers, Detectors and Associated Equipment*, 553(3):491–500, 2005.
7. G. Gilardy. Private communication, 2017.
8. E. Jones, T. Oliphant, P. Peterson, et al. SciPy: Open source scientific tools for Python, 2001–. URL <http://www.scipy.org/>. [Online; accessed 2017-03-29].
9. A. Kontos, D. Schrmann, C. Akers, M. Couder, J. Ggres, D. Robertson, E. Stech, R. Talwar, and M. Wiescher. *Nuclear Instruments and Methods in Physics Research Section A: Accelerators, Spectrometers, Detectors and Associated Equipment*, 664(1):272 – 281, 2012. doi: <https://doi.org/10.1016/j.nima.2011.10.039>.

10. K. Makino and M. Berz. *Nuclear Instruments and Methods in Physics Research, Section A: Accelerators, Spectrometers, Detectors and Associated Equipment*, 558 (1):346–350, 3 2006. ISSN 0168-9002. doi: 10.1016/j.nima.2005.11.109.
11. Z. Meisel, K. Shi, A. Jemcov, and M. Couder. *Nuclear Instruments and Methods in Physics Research, Section A: Accelerators, Spectrometers, Detectors and Associated Equipment*, 828:8–14, 2016. doi: 10.1016/j.nima.2016.04.115.
12. Z. Meisel, M. T. Moran, G. Gilardy, J. Schmitt, C. Seymour, and M. Couder. *Nuclear Instruments and Methods in Physics Research Section A: Accelerators, Spectrometers, Detectors and Associated Equipment*, 850:48 – 53, 2017. doi: <http://dx.doi.org/10.1016/j.nima.2017.01.035>.
13. L. Morales, S. Kalkal, H. S. Jung, C. Seymour, G. Gilardy, M. Moran, Z. Meisel, J. Hinnefeld, and M. Couder. Performance of the st. george detector system. In *APS Division of Nuclear Physics Meeting Abstracts*, 2016. URL <http://meetings.aps.org/link/BAPS.2016.DNP.PC.7>.
14. J. A. Nelder and R. Mead. *The Computer Journal*, 7(4):308–313, 1965.
15. J. F. Ziegler, J. P. Biersack, and M. D. Ziegler. Srim-2008.04, 2008. URL <http://www.srim.org/>.

<p><i>This document was prepared & typeset with pdfL^AT_EX, and formatted with NDdiss2_ε classfile (v3.2013[2013/04/16]) provided by Sameer Vijay and updated by Megan Patnott.</i></p>
